Acta Pharmaceutica Sinica B 2026;16(7):4166−4195

Chinese Pharmaceutical Association
Institute of Materia Medica, Chinese Academy of Medical Sciences

Acta Pharmaceutica Sinica B

www.elsevier.com/locate/apsb
www.sciencedirect.com

ORIGINAL ARTICLE

Computation-driven discovery of novel chromone derivatives for the treatment of triple-negative breast cancer *via* mTOR-targeted inhibition and triggering antitumor immunity

Ji-Quan Zhang[a,*,†], Nana Zhang[a,b,†], Yunsheng Ran[a,†], Qi-Ying Yu[c,†], Jiangrong Lu[a], Rui Chen[a], Shipeng Zhang[d], Yongxi Dong[a], Rong-Hua Wang[a], Yuanyong Yang[a], Yuanyuan Li[a], Weike Liao[a], Ling Wang[d,*], Changyou Zhan[b,*], Lei Tang[a,*]

[a]*State Key Laboratory of Discovery and Utilization of Functional Components in Traditional Chinese Medicine, Guizhou Provincial Engineering Technology Research Center for Chemical Drug R&D, School of Pharmaceutical Sciences, Guizhou Medical University, Guiyang 561113, China*
[b]*Department of Pharmacy, Shanghai Pudong Hospital & Department of Pharmacology, School of Basic Medical Sciences, Fudan University, Shanghai 200032, China*
[c]*Tumor Hospital Affiliated to Nantong University, Nantong 226361, China*
[d]*School of Biology and Biological Engineering, South China University of Technology, Guangzhou 510006, China*

Received 22 April 2025; received in revised form 28 June 2025; accepted 17 August 2025

KEY WORDS

Triple-negative breast cancer;
Mammalian target of rapamycin;
Artificial intelligence-assisted drug design;
Structure-based drug

Abstract Triple-negative breast cancer (TNBC) is a highly aggressive and heterogeneous subtype of breast cancer characterized by early metastasis, poor prognosis, and high recurrence rates. Targeting dysregulated PI3K/Akt/mTOR signaling and triggering anti-tumor immunity represent promising strategies for TNBC therapy. In this study, we report the discovery of a series of novel chromone derivatives as potent mTOR inhibitors by artificial intelligence-assisted drug design and structure-based drug design. The optimal compound, **MT-44**, was a highly selective mTOR inhibitor and showed no obvious binding activity to a broad panel of 200 kinases, and it exhibited nanomolar-level mTOR inhibitory and anti-TNBC cells proliferative activities. **MT-44** effectively blocked the PI3K/Akt/mTOR signaling pathway

This article is part of special issue entitled Machine Learning in Drug Discovery.

*Corresponding authors.
E-mail addresses: zjqgmc@163.com (Ji-Quan Zhang), lingwang@scut.edu.cn (Ling Wang), cyzhan@fudan.edu.cn (Changyou Zhan), tlei1974@163.com (Lei Tang).
[†]These authors made equal contributions to this work.

Peer review under the responsibility of Chinese Pharmaceutical Association and Institute of Materia Medica, Chinese Academy of Medical Sciences.

https://doi.org/10.1016/j.apsb.2025.09.010

design;
Targeted therapy;
Immunotherapy;
Autophagy;
Structure−activity relationship

and exerted robust anti-tumor efficacy in an MDA-MB-231 xenograft mouse model. Furthermore, **MT-44** activated pattern recognition receptor TLR2 and upregulated the cGAS/STING signaling pathway, and reshaped the tumor microenvironment, thereby enhancing the tumor immune landscape. Collectively, our findings highlighted **MT-44** as a highly selective and potent mTOR inhibitor with dual-targeted therapeutic and immunomodulatory effects, offering an appealing strategy for TNBC.

1. Introduction

Triple-negative breast cancer (TNBC) is a highly aggressive subtype of breast cancer (BC), accounting for about 15%−20% of newly diagnosed BC cases and with over 50% mortality[1-3]. TNBC is characterized by the lack of expression of the three main BC biomarkers, namely, estrogen receptors (ERs), progesterone receptors (PRs), and human epidermal growth factor receptor 2 protein (HER2), according to immunohistochemical examination results of cancer tissue[2,3]. Therefore, TNBC is typically insensitive to hormonal therapy or HER2-targeted treatment that is normally used in most other BC patients, and cytotoxic chemotherapy with relatively limited efficiency, severe side reactions, and a high relapse rate still stands as the main therapeutic option. Although some small-molecule candidates targeting diverse kinases or proteases, such as EGFR, PARP, CDKs, MEK, and PI3K/Akt/mTOR signaling pathway inhibitors (Fig. 1), have been developed for the potential monotherapy or combination drug strategy for TNBC[4], low objective response rates and limited clinical benefits were achieved. Because of the high incidence, poor prognosis, and low survival rate, the development of effective targeted inhibitors for the treatment of TNBC faces a great challenge and thus constitutes a huge clinical demand.

The phosphoinositide 3-kinase (PI3K) −protein kinase B (Akt) −mammalian target of rapamycin (mTOR) pathway plays vital roles in cellular growth, proliferation, differentiation, and survival[5,6]. PI3Ks transduce the cellular signals from G protein-coupled receptors and receptor tyrosine kinases and activate the key downstream signaling proteins Akt and mTOR by catalyzing the formation of the secondary messenger phosphatidylinositol (3,4,5)-triphosphate from phosphatidylinositol (4,5)-biphosphate. The mTOR belongs to a group of serine-threonine protein kinases of the PI3K superfamily and exists in two distinct complexes: mTOR complex 1 (mTORC1) and mTOR complex 2 (mTORC2), which play different biological functions in cell maintenance[6]. The overactivation of mTORC1 leads to a wide range of precancerous effects, including cell cycle progression, proliferation, and survival; whereas dysregulation of mTORC2 affects Akt phosphorylation and cytoskeleton protein functions. S6K1 (p70S6 kinase) and 4E-BP1 (4E-binding protein) are key downstream effectors of mTORC1, which are critically involved in the regulation of protein synthesis[7]. It has been confirmed that the abnormal activation of the mTOR pathway is closely related to the survival and progression of TNBC[8-10], suggesting that mTOR inhibition may become a potential strategy for the treatment of TNBC.

It has been confirmed that mTOR inhibition is closely related to anti-tumor immunity in TNBC by increasing T-cell activity and IFN-γ responses[8,11]. Compared with "cold tumors" where the immune response is dormant, the effects of drug chemotherapy, radiation, and immunotherapy are significantly enhanced in "hot tumors" where immune cells are active[12]. One critical mechanistic strategy involves activating the cGAS/STING signaling pathway to enhance innate immune surveillance and remodel the tumor microenvironment[13-15]. STING activation triggers the downstream TANK-binding kinase 1 and interferon regulatory factor 3 (IRF3) signaling cascade, culminating in the production of type I interferons and the infiltration of anti-tumor immune cells[16-18]. Notably, Toll-like receptors (TLRs), as pattern recognition receptors, serve as key sentinels of the innate immune system. They regulate innate immunity and subsequent adaptive immune responses, playing a pivotal role in cancer immunotherapy[19]. Unlike other molecular subtypes of breast cancer, TNBC exhibits elevated PD-L1 expression and significant immune infiltration, suggesting a potential benefit from immunotherapy[20]. However, the limited presence of tumor-infiltrating effector lymphocytes severely compromises clinical efficacy. Therefore, the combination of mTOR-targeted inhibition with STING and TLR2 pathways activation represents a highly attractive therapeutic strategy against TNBC, offering enhanced clinical benefits for patients.

Hitherto, structurally diverse mTOR inhibitors have been developed, including allosteric mTOR inhibitors and ATP-competitive mTOR inhibitors, some of which have been systematically investigated in the treatment of TNBC[4,21]. For example, Everolimus (Fig. 1), a hydroxyethyl derivative of Rapamycin belonging to the macrolide allosteric mTOR inhibitors, has been intensively evaluated in multiple clinical trials for the treatment of TNBC and metastatic TNBC (NCT02456857, NCT05954442 and NCT00930930), and showed promising clinical efficacy along with acceptable side reactions[22,23]. As the first synthetic pan-PI3K/mTOR inhibitor, **PI-103** was proven to enhance radiation-induced cell death in BRCA-proficient MDA-MB-435S and MDA-MB-231-BR cells and xenografts in combination with Olaparib (a PARP inhibitor, Fig. 1)[24], and the dual PI3K/mTOR inhibitor BEZ-235 combined with CAPE can effectively inhibit tumor metastasis and progression in TNBC cells[25]. MNL-0128 is a potent and selective mTOR inhibitor developed by Takeda, which has been clinically evaluated for the potential treatment of TNBC and showed good anti-tumor activity and drug tolerance[26] (Fig. 1). Despite structurally diverse ATP-competitive mTOR inhibitors have been developed and some of these candidates have advanced to the clinical trials, no agents have been approved by the FDA due to their low kinase selectivity, poor drug-likeness profiles, and unfavorable on- and off-target side effects[27]. Notably, our recent systemic bioinformatics analysis of the gene expression with prognostic survival of TNBC patients showed that the expression level of EIF4EBP1 was closely related to the overall survival and disease-free survival of TNBC (Fig. 2), which further confirms that the development of a highly selective mTOR inhibitor is a practical and urgent strategy for TNBC treatment.

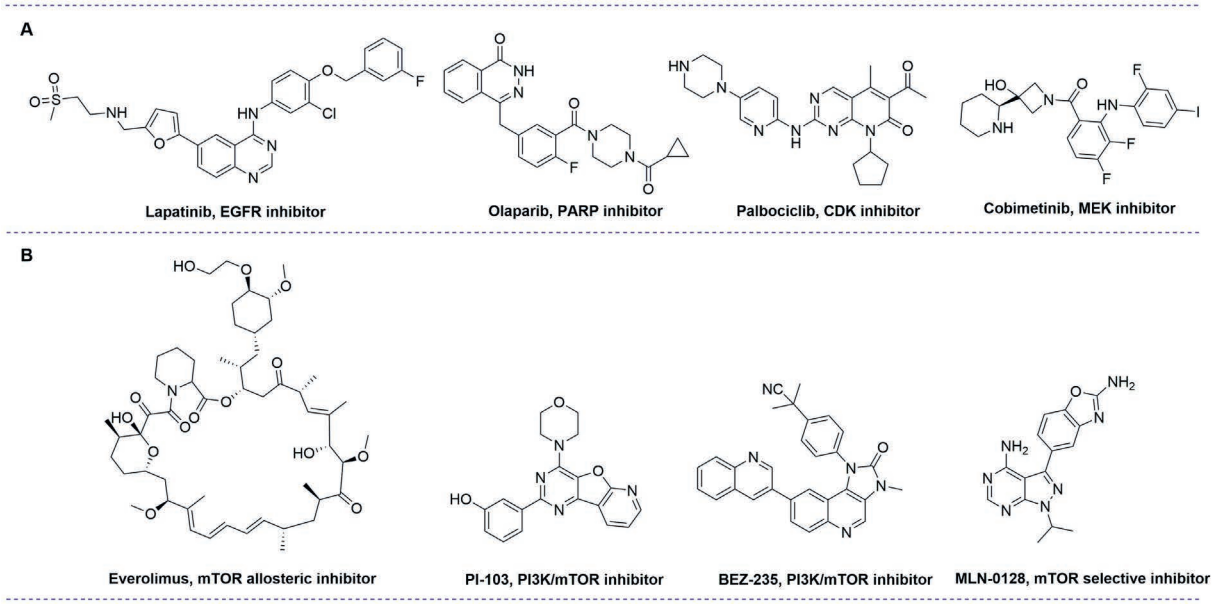

Figure 1 Clinical candidates for the potential treatment of TNBC. (A) FDA-approved small molecule inhibitors, (B) PI3K/Akt/mTOR signaling pathway inhibitors.

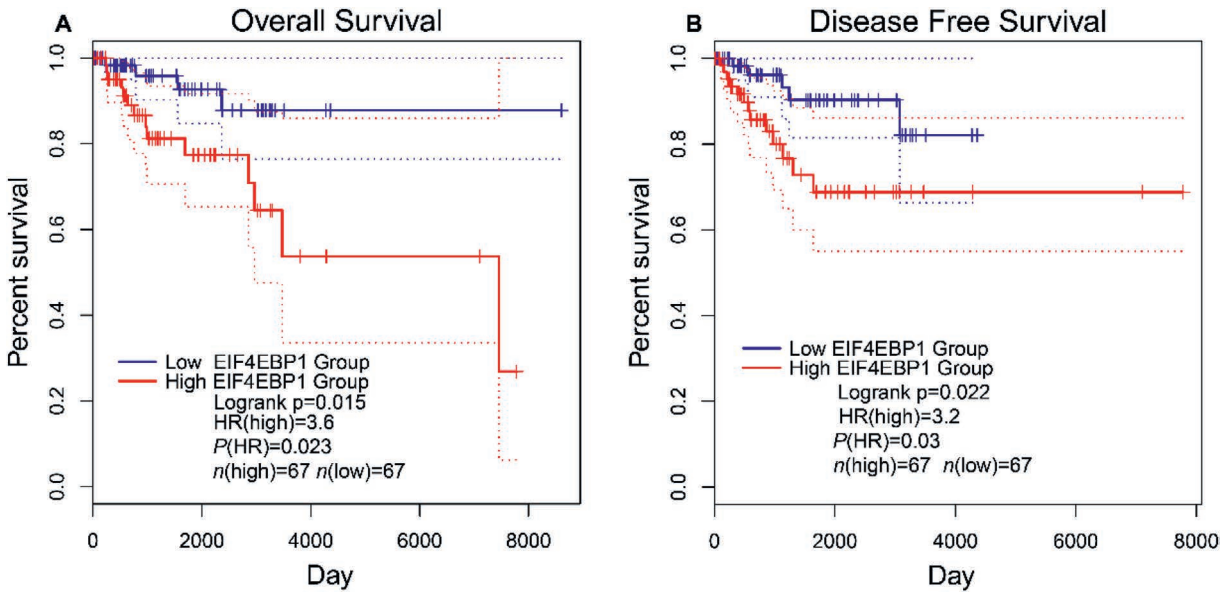

Figure 2 Bioinformatics analysis of gene expression in triple-negative breast cancer patients and their overall survival (A), and disease-free (B) progression periods.

On this basis, it is critical to expedite the discovery and development of novel mTOR inhibitors possessing new scaffold structures with high potency, aiming to advance therapeutic options for TNBC. Artificial intelligence (AI)-driven drug design has revolutionized the discovery of lead compounds by enabling rapid virtual screening of vast chemical libraries and *de novo* molecular generation with optimized drug-likeness. Machine learning models, trained on high-throughput screening data and structural biology insights, can identify novel chemotypes with high affinity for therapeutic targets while minimizing off-target effects[28-30]. Deep generative adversarial networks further accelerate scaffold hopping, creating chemically diverse analogues that bypass existing intellectual property constraints[31]. Because of the continued interest in exploring highly active kinase inhibitors based on the PI3K/Akt/mTOR pathway[32-36], our recent medicinal work on the development of highly potent and selective mTOR inhibitors *via* AI-assisted drug design (AIDD) and structure-based drug design (SBDD) strategies facilitated the discovery of a novel chromone-based derivative, **MT-44**, for the potential therapy of TNBC *via* mTOR-targeted inhibition and cGAS/STING pathway activation.

2. Results and discussion

2.1. *Discovery of the lead compound **MT-1** (Table 1, **4a**)*

Virtual screening is a very practical and efficient strategy for finding structurally novel and potentially bioactive lead compounds. To begin our medicinal campaign, the ligand **PI-103** was taken as the shape molecule, and approximately 1.5 million molecules in the ChemDiv database were used to perform a shape screening *via* the Shape Screening workflow of Schrödinger software (Fig. 3A). The Pharmacophore Types, as volume scoring, wrote out at most 1 alignment per ligand and filtered out conformers with similarity below 0.8. Machine learning can deliver excellent performance in the virtual screening domain[37]. Therefore, the remaining ligands after shape screening were selected to predict active score in models with better predictive performance that were built *via* machine learning algorithms (Random Forest, XGBoost), the ligands with a prediction label of "1" were docked to the mTOR protein to improve the hit rate. Conformers with similarity below 0.8 compared with **PI-103** were filtered out, and then the remaining ligands were selected to predict active score in models with better predictive performance that were built *via* machine learning algorithms (Random Forest, XGBoost), the ligands with a prediction label of "1" were docked to the mTOR protein (PDB: 4JT6). Subsequently, a cluster analysis was performed, and the optimal ligand **MT-1** (**4a**) was screened out with the highest docking score and model predictive score, which contained a chromone scaffold with an imine substituent at the C-4 position. Then, **MT-1** was synthesized and its *in vitro* kinase inhibitory activity was confirmed with an IC_{50} value of 1.5 μmol/L against mTOR (Fig. 3A).

2.2. *Molecular design based on **MT-1***

To develop novel potent and selective mTOR inhibitors, the binding patterns of **PI-103** and **MT-1** with the mTOR protein were investigated using molecular docking and molecular dynamics simulations. As shown in Fig. 3B, the oxygen atom on the morpholine ring of **PI-103** formed a key hydrogen bond interaction with residue Val-2240 (1.8 Å), the hydroxyl group from the benzene ring formed two hydrogen bond interactions with residues Tyr-2225 (2.7 Å) and Asp-2195 (2.3 Å). Compared with **PI-103**, **MT-1** indicated no interaction with residues Tyr-2225 and Asp-2195, and only the hydrogen bond interaction between the oxygen atom on the pepper ring and residue Val-2240 (2.1 Å). The molecular dynamics simulations of **MT-1** with the mTOR protein complex were performed to further verify the stability of the docking conformation. As shown in Fig. 3C, we aligned conformations extracted from the dynamic simulation trajectory to the docking conformation, and the conformations extracted from the dynamic simulation trajectory were consistent with the docking conformation. Guided by these binding modes, we performed the first round of structure-activity relationship (SAR) explorations based on **MT-1** to improve the kinase inhibitory activity: (1) the R^1 group of **MT-1** toward the solvent-exposed area of the protein pocket, thus various amino acids in different lengths, such as alanine, morpholine, and L-prolinamide, were introduced to enhance the interaction with the surrounding residues. Meanwhile, side chain substituents on the *meta*- or *para*-positions were also modestly investigated. (2) Substituents on the R^2 and R^3 areas orient to the affinity pocket, and diverse groups, such as F, methoxy, amino, and nitro groups, were investigated to increase additional hydrogen bond

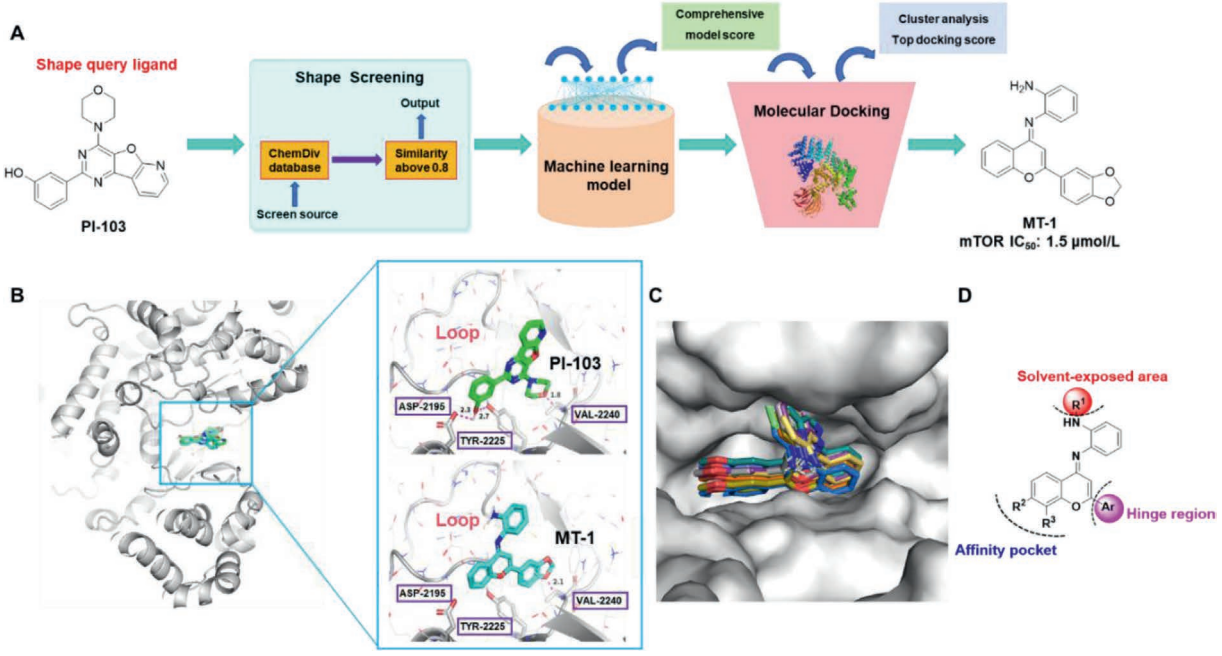

Figure 3 (A) Screening flow of mTOR inhibitors and discovery of **MT-1**. (B) Comparison of binding modes of **PI-103** and **MT-1** with mTOR protein (PDB: 4JT6). (C) Align conformations extracted from the dynamic simulation trajectory to the docking conformation of **MT-1**. The conformations extracted from the dynamic simulation trajectory are consistent with the docking conformation. (D) The pocket analysis of **MT-1** with mTOR protein guided by binding modes.

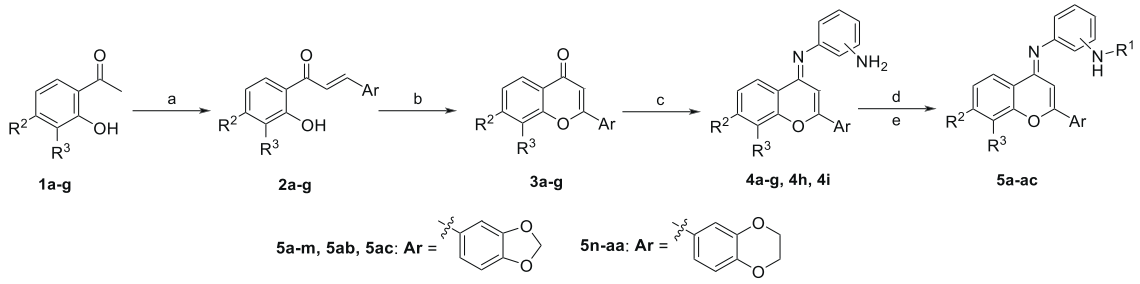

5a: R^1 = 2-aminoacetyl, R^2 = H, R^3 = H
5b: R^1 = (*S*)-2-aminopropionyl, R^2 = H, R^3 = H
5c: R^1 = (*S*)-3-amino-3-hydroxypropionyl, R^2 = H, R^3 = H
5d: R^1 = 3-methoxypropionyl, R^2 = H, R^3 = H
5e: R^1 = 3-aminopropionyl, R^2 = H, R^3 = H
5f: R^1 = 4-aminobutyryl, R^2 = H, R^3 = H
5g: R^1 = 5-aminovaleryl, R^2 = H, R^3 = H
5h: R^1 = 1-morpholineformyl, R^2 = H, R^3 = H
5i: R^1 = piperazineformyl, R^2 = H, R^3 = H
5j: R^1 = (*S*)-2-amino-3,3-dimethylbutyryl, R^2 = H, R^3 = H
5k: R^1 = (*S*)-2-amino-3,3-dimethylbutyryl, R^2 = MeO, R^3 = H
5l: R^1 = 2-aminoacetyl, R^2 = H, R^3 = NO_2
5m: R^1 = 2-aminoacetyl, R^2 = H, R^3 = NH_2
5n: R^1 = 1-morpholineformyl, R^2 = F, R^3 = H
5o: R^1 = 1-pyrrolidine-2-carboxamide-formyl, R^2 = F, R^3 = H
5p: R^1 = 2-aminoacetyl, R^2 = H, R^3 = H
5q: R^1 = (*S*)-2-aminopropionyl, R^2 = H, R^3 = NO_2
5r: R^1 = (*S*)-2-aminopropionyl, R^2 = H, R^3 = NH2
5s: R^1 = (*S*)-2-aminopropionyl, R^2 = MeO, R^3 = H
5t: R^1 = 2-aminoacetyl, R^2 = MeO, R^3 = H
5u: R^1 = (*S*)-3-amino-3-hydroxypropionyl, R^2 = MeO, R^3 = H
5v: R^1 = (*S*)-2-amino-3,3-dimethylbutyryl, R^2 = MeO, R^3 = H
5w: R^1 = 1-morpholineformyl, R^2 = MeO, R^3 = H
5x: R^1 = (*S*)-2-aminopropionyl, R^2 = F, R^3 = H
5y: R^1 = 2-aminoacetyl, R^2 = F, R^3 = H
5z: R^1 = 3-aminopropionyl, R^2 = F, R^3 = H
5aa: R^1 = (*S*)-2-amino-3,3-dimethylbutyryl, R^2 = F, R^3 = H
5ab: R^1 = 3-aminopropionyl, R^2 = H, R^3 = H
5ac: R^1 = 3-aminopropionyl, R^2 = H, R^3 = H

Scheme 1 Synthetic route for compounds **4a** and **5a**−**ac**. Reagents and conditions: (a) piperonyl aldehyde or 1,4-benzodioxin-6-carboxaldehyde, 20% NaOH, EtOH, room temperature (rt), 24 h, 72%−90%; (b) I_2, DMSO, 150 °C, 1 h, 72%−87%; (c) *ortho*-, *meta*-, or *para*-phenylenediamine, $Ti(OEt)_4$, toluene, 120 °C, 20 h, 63%−76%; (d) diverse substituted amines, phenyl chloroformate, pyridine, rt, 12 h or diverse carboxylic acids, HATU, DIPEA, DMF, rt, 12 h; (e) TFA, DCM, rt, 6 h and Fe powder, NH_4Cl, EtOH/H_2O (*v*:*v* = 1:1), 90 °C, 5 h, 33%−68% (d and e).

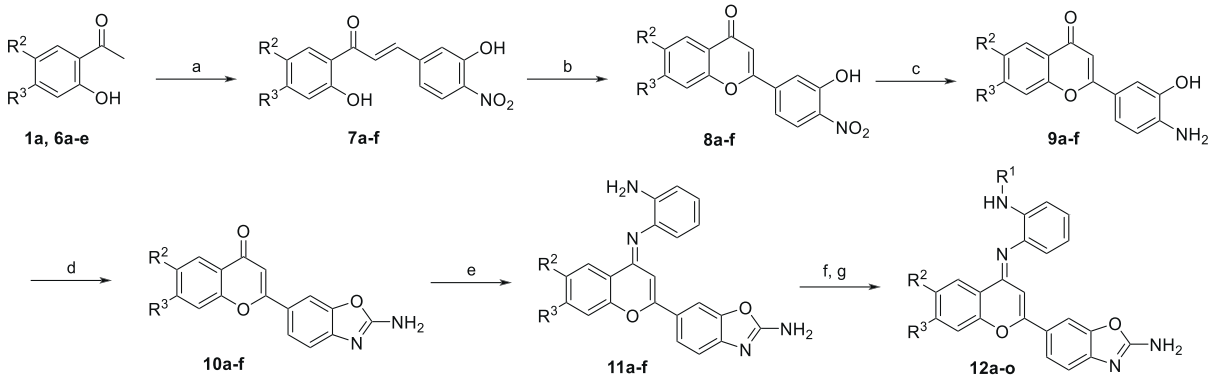

12a: R^1 = 3-aminopropionyl, R^2 = H, R^3 = H
12b: R^1 = 3-methoxypropionyl, R^2 = H, R^3 = H
12c: R^1 = 3-methylaminopropionyl, R^2 = H, R^3 = H
12d: R^1 = 3-methanesulfonamidepropionyl, R^2 = H, R^3 = H
12e: R^1 = 3-dimethylaminopropionyl, R^2 = H, R^3 = H
12f: R^1 = 3-diethylaminopropionyl, R^2 = H, R^3 = H
12g: R^1 = 3-tetrahydropyrrolidinepropionyl, R^2 = H, R^3 = H
12h: R^1 = 3-morpholinepropionyl, R^2 = H, R^3 = H
12i: R^1 = 3'-tetrahydropyrrolidineformyl, R^2 = H, R^3 = H
12j: R^1 = 3-aminopropionyl, R^2 = MeO, R^3 = H
12k: R^1 = 3-aminopropionyl, R^2 = F, R^3 = H
12l: R^1 = 3-aminopropionyl, R^2 = CN, R^3 = H
12m: R^1 = 3-aminopropionyl, R^2 = H, R^3 = OH
12n: R^1 = 3-aminopropionyl, R^2 = OH, R^3 = H
12o: R^1 = 3-aminopropionyl, R^2 = H, R^3 = Br

Scheme 2 Synthetic route for compounds **12a**−**o**. Reagents and conditions: (a) 3-hydroxy-4-nitrobenzaldehyde, 20% NaOH, EtOH, 24 h, rt, 63%−81%; (b) I_2, DMSO, 150 °C, 1 h, 48%−74%; (c) Fe powder, NH_4Cl, EtOH/H_2O (*v*:*v* = 1:1), 90 °C, 25%−56%; (d) BrCN, MeOH, rt, 24 h, 26%−60%; (e) *ortho*-phenylenediamine, $Ti(OEt)_4$, toluene, 120 °C, toluene, 19%−42%; (f) diverse carboxylic acids, HATU, DIPEA, DMF, rt, 12 h; (g) TFA, DCM, rt, 6 h and BBr_3, DCM, −78 °C−rt, 12 h, 27%−66% (f and g).

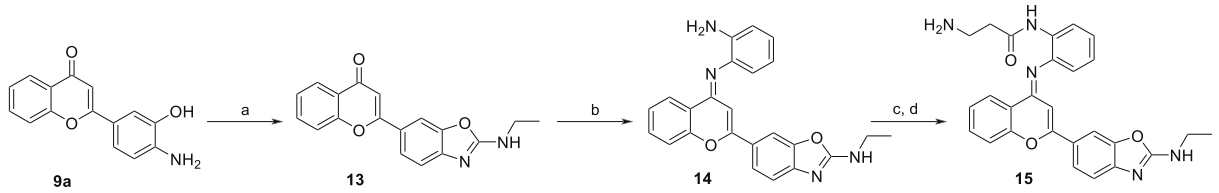

Scheme 3 Synthesis of compound **15**. Reagents and conditions: (a) EDCI, isopropanol, 85 °C, 18 h, 52%; (b) *ortho*-phenylenediamine, $Ti(OEt)_4$, toluene, 120 °C, 20 h, 41%; (c) Boc-β-alanine, HATU, DIPEA, DMF, rt, 12 h; (d) TFA, DCM, rt, 6 h, 39% (c and d).

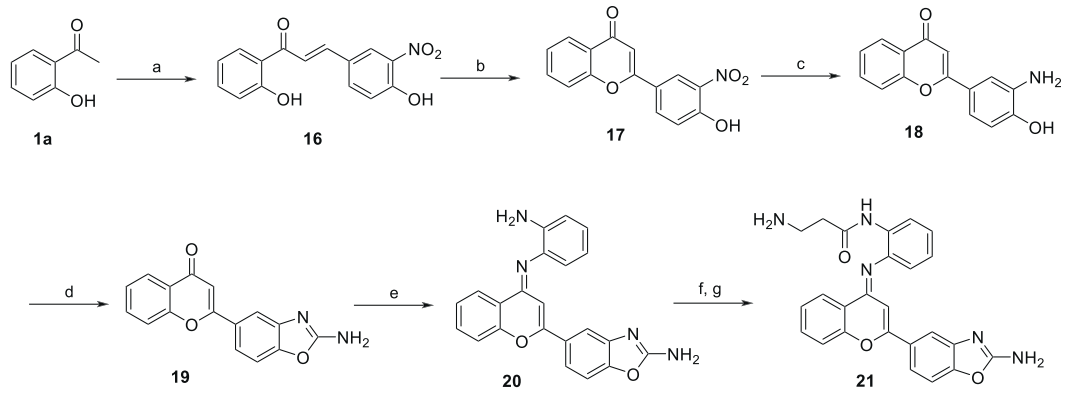

Scheme 4 Synthesis of compound **21**. Reagents and conditions: (a) 3-nitro-4-hydroxybenzaldehyde, 20% NaOH, EtOH, 24 h, rt, 73%; (b) I_2, DMSO, 150 °C, 2 h, 62%; (c) Fe powder, NH_4Cl, $EtOH/H_2O$ ($v:v$ = 1:1), 90 °C, 5 h, 55%; (d) BrCN, MeOH, rt, 24 h, 54%; (e) *ortho*-phenylenediamine, $Ti(OEt)_4$, toluene, 120 °C, 20 h, 39%; (f) *Boc*-β-alanine, HATU, DIPEA, DMF, rt, 12 h; (g) TFA, DCM, rt, 6 h, 48% (f and g).

interaction with residue Asp-2195 or Tyr-2225. (3) Considering the metabolic instability of the pepper ring and its farther distance away from the key residue Val-2240 compared with that of **PI-103**, different aromatic ring groups were designed and evaluated (Fig. 3D).

2.3. *Chemical synthesis*

The designed target compounds were prepared *via* four synthetic routes (Schemes 1−4). The procedure for compounds with 1,3-benzodioxole (pepper ring) and 1,4-benzodioxine substituents on the C-2 position is outlined in Scheme 1. Compounds **4a** and **5a**−**ac** were synthesized from substituted 2-hydroxyacetophenone by five steps of transformation, namely aldol condensation, free radical cyclization, imine formation, amidation, and final deprotection. It should be noted that the synthesis of imine intermediates **4a**−**g**, **4h**, and **4i** from **3a**−**g** under strong Lewis acid $Ti(OEt)_4$-catalyzed conditions was the key step, and only moderate yields were obtained (63%−76%). A similar route with Scheme 1 was developed for the synthesis of C-2 benzoxazole motif-substituted derivatives **12a**−**o** (Scheme 2), the main difference lay in the formation of amino-substituted benzoxazole, which was obtained by condensation of 2-aminophenol with BrCN in low to moderate yields (26%−60%).

Scheme 3 shows the procedure for the synthesis of compound **15**. Starting from 2-aminophenol-substituted intermediate **9a, 13** was prepared by condensation with EDCI in isopropanol conditions. Then, **13** underwent imidization and subsequent amide condensation and deprotection to produce the desired compound **15**. Compound **21** was synthesized using a similar procedure to **12a**, and 4-hydroxy-3-nitrobenzaldehyde was used in the aldol condensation reaction (Scheme 4).

2.4. *SAR discussion*

Our primary structural modification on **MT-1** focused on the R^1 substituent, and diverse amide side chains were introduced (Table 1), such as simple amino acids and alkoxycarboxylic acid (**5a**−**d**, **5j**), finding that the glycine-substituted derivative **5a** showed an increase in kinase inhibitory activity with an IC_{50} value of 719.0 nmol/L. Then, different carbon chain lengths between the free amino and carbonyl groups were investigated (**5e**−**g**), and the results indicated that β-aminopropionic acid was the optimal substituent, and the corresponding compound **5e** exhibited an inhibitory IC_{50} of 316.6 nmol/L against mTOR (Table 1). We analyzed the binding postures of **5a** (Fig. 4A) and **5e** (Fig. 4B) in the mTOR binding pocket, and the results showed that compared with **5a**, the β-alanine substituted on the R^1 site of **5e** formed two key hydrogen bond interactions with residues Asn-2343 and Asp-2357. The heterocycles, including morpholine and piperazine substituents, showed no contribution to mTOR inhibition (**5h** and **5i**). Unexpectedly, the mTOR inhibitory activity was completely lost when the pepper ring was replaced with 1,4-benzodioxole on the C-2 position (**5q**−**t**, **5x**−**y**), indicating that the structural replacement may hinder the key hydrogen bond interaction with residue Val-2240 in the hinge region (Fig. 4). The β-alanine attached to the *m*- or *p*-position displayed no obvious kinase inhibition against mTOR (**5 ab** and **5ac**), indicating the substituted side chain may form a key interaction with the binding pocket. Notably, when the pepper ring was replaced with 2-aminobenzoxazole, a structural motif frequently used in PI3K/

Akt/mTOR pathway inhibitors[38,39], the desired compound **12a** exhibited a significantly increased mTOR inhibitory activity with an IC_{50} value of 45.2 nmol/L, which was 34-fold more potent than the lead compound **MT-1** (Table 1). To understand further the protein-ligand interaction, the binding modes of **12a** with the ATP-binding pocket of mTOR were investigated by molecular docking. As shown in Fig. 4C, the 2-aminobenzoxazole motif formed three key hydrogen bond interactions with residues Val-2240 and Cys-2243. In addition, the electrical distribution of **12a** in the binding pocket was investigated. As shown in Fig. 4D, the benzene ring of the chromone scaffold was in a negatively charged space, and a negatively charged substituent may lead to electrostatic repulsion. With these insights in hand, the second round of the SAR study based on **12a** was performed.

In view of the key hydrogen bond interactions with the hinge region of the binding pocket and the crucial role in the kinase inhibitory activity it plays, the 2-aminobenzoxazole motif was maintained, and the structural optimization was focused on the R^1, R^2, and R^3 groups. As shown in Table 2, various substituents on the primary amine were evaluated (**12b**−**i**), and a remarkable decrease in enzyme activity was noticed when it was replaced with methoxyl, methylamino, and methanesulfonylamino

Table 1 The mTOR inhibition of chromone derivatives with benzodioxole or benzodioxan substituents.

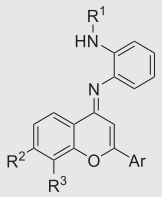

Compd.	R^1	R^2	R^3	Ar	mTOR, IC_{50} (nmol/L) [a]
4a (MT-1)	H	H	H		1539.0 ± 21.1
5a		H	H		719.0 ± 7.4
5b		H	H		3186.0 ± 194.0
5c	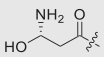	H	H		>10,000
5d	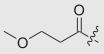	H	H		>10,000
5e	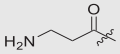	H	H		316.6 ± 19.1
5f	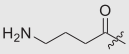	H	H		8192.0 ± 1854.0
5g	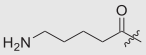	H	H	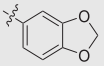	>10,000
5h		H	H		>10,000
5i		H	H		7468.2 ± 139.2
5j		H	H		>10,000
5k		OCH_3	H		NT[b]
5l		H	NO_2		NT

5m		H	NH_2		6160.0 + 1109.0
5n		F	H		NT
5o		F	H		NT
5p		H	H		1520.2 ± 121.0
5q		H	NO_2		>10,000
5r		H	NH_2		>10,000
5s		OCH_3	H		>10,000
5t		OCH_3	H		>10,000
5u	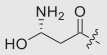	OCH_3	H	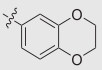	NT
5v		OCH_3	H		NT
5w		OCH_3	H		NT
5x		F	H		>10,000
5y		F	H		>10,000
5z	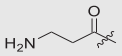	F	H		NT
5aa		F	H		NT
5ab	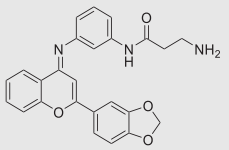				>10,000

substituents. Because of the lack of hydrogen bond interactions with residues Asp-2357 and Asn-2343, *N*,*N*-disubstituted functional groups, such as dimethylamino (**12e**, Fig. 5A), diethylamino (**12f**), pyrrolidine (**12g**), or morpholine (**12h**), showed no obvious inhibition either. However, pyrrolidine-3-carboxylic acid-substituted derivative **12i**, which could form hydrogen bond interactions with residue Gln-2167 (Fig. 5B), exhibited moderate kinase inhibitory activity with an IC_{50} value of 165.0 nmol/L. To confirm the electronic effect of substituents attached to the benzene ring of the chromone scaffold (Fig. 4D), diverse electron-withdrawing and electron-donating groups attached to R^2 and R^3 were investigated, respectively (**12j**–**o**). The electron-donating substituents, such as methoxyl and hydroxyl, were more desirable for the enzyme inhibitory activity (Fig. 5C), and compounds **12j** (**MT-44**) and **12m** showed comparable activity to **12a**, with inhibitory IC_{50} values of 49.4 and 40.2 nmol/L, respectively,

5ac	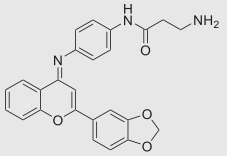	>10,000
12a	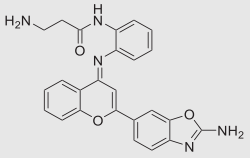	45.2 ± 8.8
PI-103	-	12.1 ± 0.6

[a]IC_{50} values are the mean ± SD of triplicate measurements. [b]NT: Not tested.

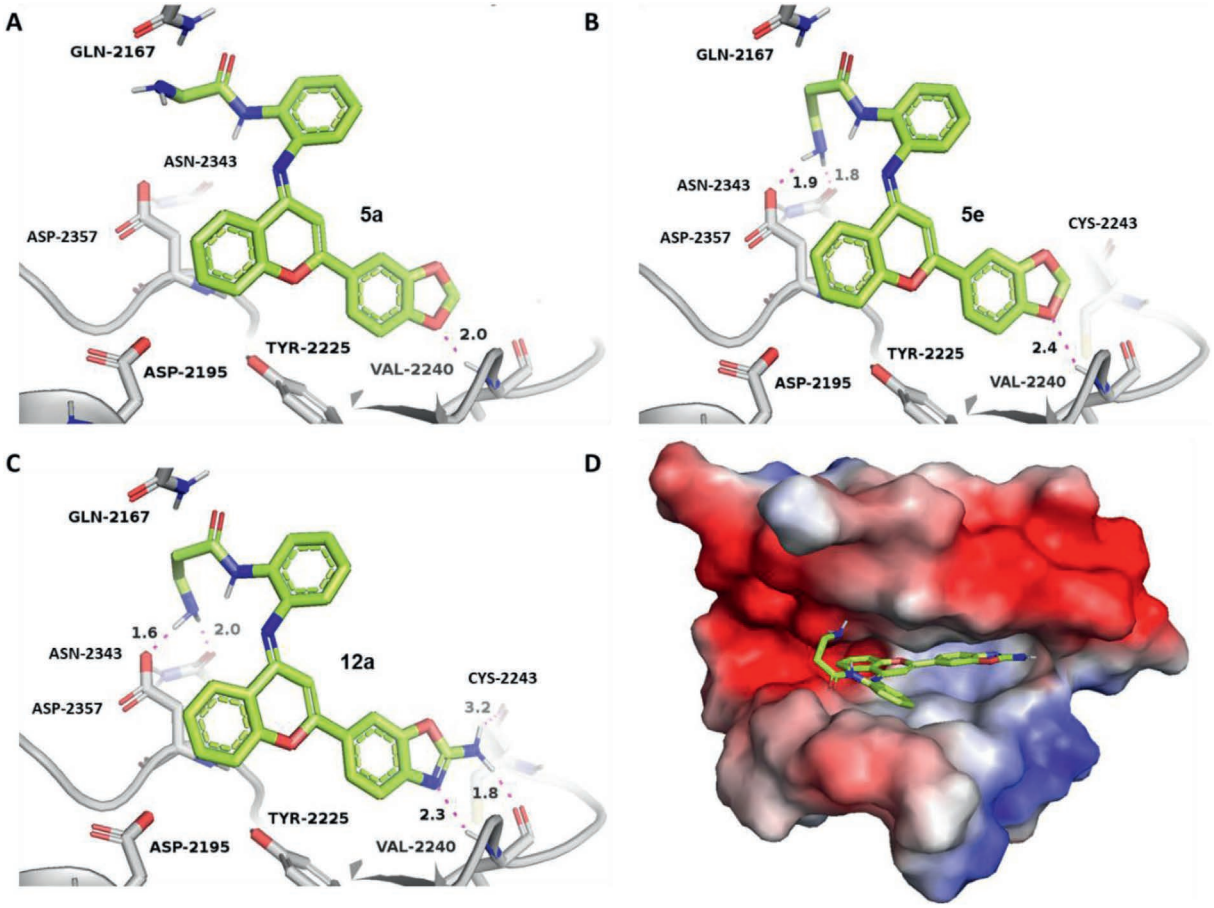

Figure 4 Binding modes of **5a** (A), **5e** (B), and **12a** (C) with mTOR (PDB: 4JT6) and electrical distribution of **12a** in the binding pocket (D). The benzene ring of the chromone scaffold lies in a negatively charged space, and a negatively charged substituent may lead to electrostatic repulsion.

indicating that an electron-donating group could better match the surrounding electronegative pocket (Fig. 4D). Notably, compound **12n** with hydroxyl substitution at R^2 that could form additional hydrogen bonding interaction with residue Glu-2190 (Fig. 5C) showed the most potent mTOR inhibitory efficacy (IC_{50}: 26.3 nmol/L), which was 1.72-fold more potent than that of **12a**. A substituent on the amino of the aminobenzoxazole motif would lose its hydrogen bonding interactions with Cys-2243 (Fig. 5D) and show a remarkable decrease in mTOR inhibition (**15**). In addition, the aminobenzoxazole attached to the C-2 of chromone *via* the C-7 position also led to a 15.4-fold decrease in kinase inhibitory activity (**21**, Table 2).

Considering the high homology of mTOR kinase with other PIKK isoforms, the subtype selectivity profiles of **12a** and **12j** (**MT-44**) were investigated aganist PI3Ks. As shown in Table 3, both compounds showed a high specificity for mTOR. To investigate the kinome-wide specificity further, we confirmed the kinase profiling of **MT-44** at a concentration of 1.0 μmol/L against a panel of 200 human kinases using the Eurofins Kinase Profiling platform (KINOMEscan). As shown in Fig. 6, **MT-44** proved to be a highly selective mTOR inhibitor and showed no obvious binding activity to this broad panel of kinases, including mTOR homologous family members and other PIKK members (only weak binding to PI3KC2γ, a member of the class II PI3K isoform). The complete profiling data of **MT-44** can be found in Supporting Information Table S1.

2.5. *In vitro cell viability*

The antiproliferative activity of the synthesized compounds was evaluated on TNBC cell lines MDA-MB-468 and MDA-MB-231, and meanwhile, breast cancer cells MCF-7, human colorectal cancer cells HCT-116, lung cancer cells A549 and H1975, and acute myeloid leukemia cells Molm-13 were also evaluated for their abnormal proliferation, which was closely related to the mTOR protein activation[40]. In general, compounds that exhibited potent kinase inhibitory activity against mTOR displayed a potent cell proliferation inhibition rate at a concentration of 1.0 μmol/L, such as **5e**, **12a**, **12c**, **12i**, **12j** (**MT-44**), and **12n**. Among these, **12a** showed a 78.5% inhibition rate against HCT-116 cells, and compound **12k** showed inhibition rates higher than 70% against MDA-MB-231, MCF-7, and HCT-116 cell lines (Supporting Information Table S2). Notably, compound **MT-44** exerted desirable antiproliferative activities against TNBC cells MDA-MB-468 and MDA-MB-231, with inhibition rates of 74.0% and 70.7%, respectively, which were much more potent than that of the positive control **PI-103** (Table S2). Then, compounds **12a**, **12c**, **12k**, **12j**, **12m**, **12n**, and **12i** were selected for further IC_{50} values confirmation on sensitive cells MDA-MB-231, MDA-MB-436, MCF-7, and HCT-116. As shown in Table 4, most of the investigated compounds showed high sensitivity to TNBC cells MDA-MB-231 and MDA-MB-436. In particular, compound **MT-44** exhibited IC_{50} values of 66.5 and 148.2 nmol/L against MDA-MB-231 and MDA-MB-468, respectively. Meanwhile, the antiproliferative activities of clinical therapeutic drugs for TNBC were also evaluated, including Everolimus, Paclitaxel, Doxorubicin, and MLN-0128, finding that the optimal compound, **MT-44**, exerted a significant advantage on sensitive cells MDA-MB-231, showing 34.4- and 1.1-fold more potent antiproliferative effect than Everolimus and Doxorubicin, respectively (Table 4).

2.6. *Anti−migration effect of compound **MT-44***

Malignant cell migration and invasion play important roles in the progression and metastasis of TNBC[41]. Therefore, the anti-

Table 2 mTOR inhibition of chromone derivatives with benzoxazole substituent.

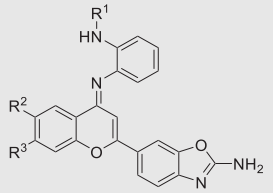

Compd.	R^1	R^2	R^3	mTOR, IC_{50} (nmol/L)[a]
12a	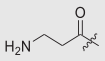	H	H	45.2 ± 8.8
12b	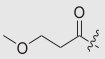	H	H	3373.2 ± 334.3
12c	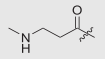	H	H	472.8 ± 42.4
12d	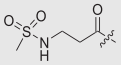	H	H	3393.2 ± 164.1
12e	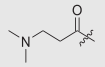	H	H	2610.0 ± 201.5
12f	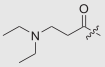	H	H	>10,000
12g	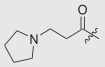	H	H	>10,000
12h	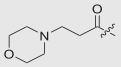	H	H	>10,000
12i	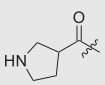	H	H	165.0 ± 8.1

12j (MT-44)	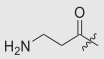	OCH_3	H	49.4 ± 17.1
12k	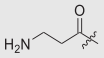	F	H	166.0 ± 6.3
12l	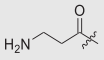	CN	H	1240.0 ± 86.1
12m	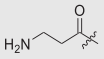	H	OH	40.2 ± 1.0
12n	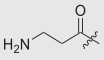	OH	H	26.3 ± 0.2
12o	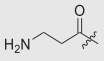	H	Br	9339.8 ± 748.4
15	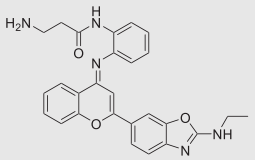			2664.5 ± 380.3
21	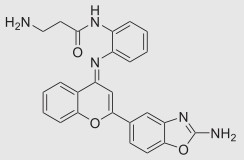			696.1 ± 58.2
PI-103	-			12.1 ± 0.6

[a]IC_{50} values are the mean ± SD of triplicate measurements.

migration effect of **MT-44** was investigated on MDA-MB-231 cells using a wound healing assay. As shown in Fig. 7A, compared with the control, **PI-103** and **MT-44** could significantly inhibit the migration of the MDA-MB-231 cells in a concentration-dependent, and compound **MT-44** showed more potent anti-migration effects than **PI-103** at the same test concentration (Fig. 7B and C). In addition, the protein expression inhibitory effect of **MT-44** on cell migration has also been evaluated. As shown in Fig. 7D and E, the expression level of vimentin, a key protein that is critical for tumor cell migration and metastasis, was significantly inhibited in a concentration-dependent manner following treatment with compound **MT-44**.

*2.7. Compound **MT-44** inhibits the colony formation and invasion of MDA-MB-231 cells*

Tumor cell proliferation and invasion are crucial for tumor progression and metastasis[42]. To investigate further the anti-proliferative potential, a colony formation assay was performed to determine the long-term effects of the optimal compound, **MT-44**, on MDA-MB-231 cells (Fig. 8A and B). The results indicated that the colony formation ability of MDA-MB-231 cells was significantly inhibited after treatment with **PI-103** and **MT-44**, and the inhibitory effect of **MT-44** was much more potent than that of **PI-103** at the same concentration. Additionally, **PI-103** and **MT-44** were detected in MDA-MB-231 cell lines using a Transwell assay. Fig. 8C and D shows that **MT-44** could significantly inhibit the invasion of the MDA-MB-231 cells in a concentration-dependent manner when compared with the control **PI-103**, and the inhibitory effect was more potent than with **PI-103** at the same concentration.

*2.8. Cell cycle arrest effects of compound **MT-44***

Flow cytometric analysis was employed to evaluate the effects of **PI-103** and **MT-44** on cell cycle progression. In the control group, the distribution of cells across the G0/G1, S, and G2/M phases was 44.79%, 50.01%, and 5.20%, respectively (Fig. 9A). Treatment with increasing concentrations of **MT-44** (0.25, 0.5, and 1 μmol/L) resulted in a progressive accumulation of cells in the G0/G1 phase (49.35% to 52.38%), a reduction in the S phase population (45.15% to 29.77%), and a significant increase in the G2/M phase population (5.48% to 17.84%). By contrast, **PI-103** exhibited weak effects on cell cycle distribution (Fig. 9A), potentially correlated with its lower antitumor activity (Table 4). These findings demonstrated that **MT-44** induced G2/M phase arrest in MDA-MB-231 cells, effectively inhibiting tumor cell proliferation. Compared with **PI-103**, **MT-44** exerted a more pronounced effect on cell cycle arrest (Fig. 9B and C). Furthermore, the expression levels of CDK1 and Cyclin B1, two proteins that are closely related to the G2/M phase, were also significantly decreased in Western blot analysis (Fig. 7D and E), which further confirmed that compound **MT-44** induced cell cycle arrest in the G2/M phase.

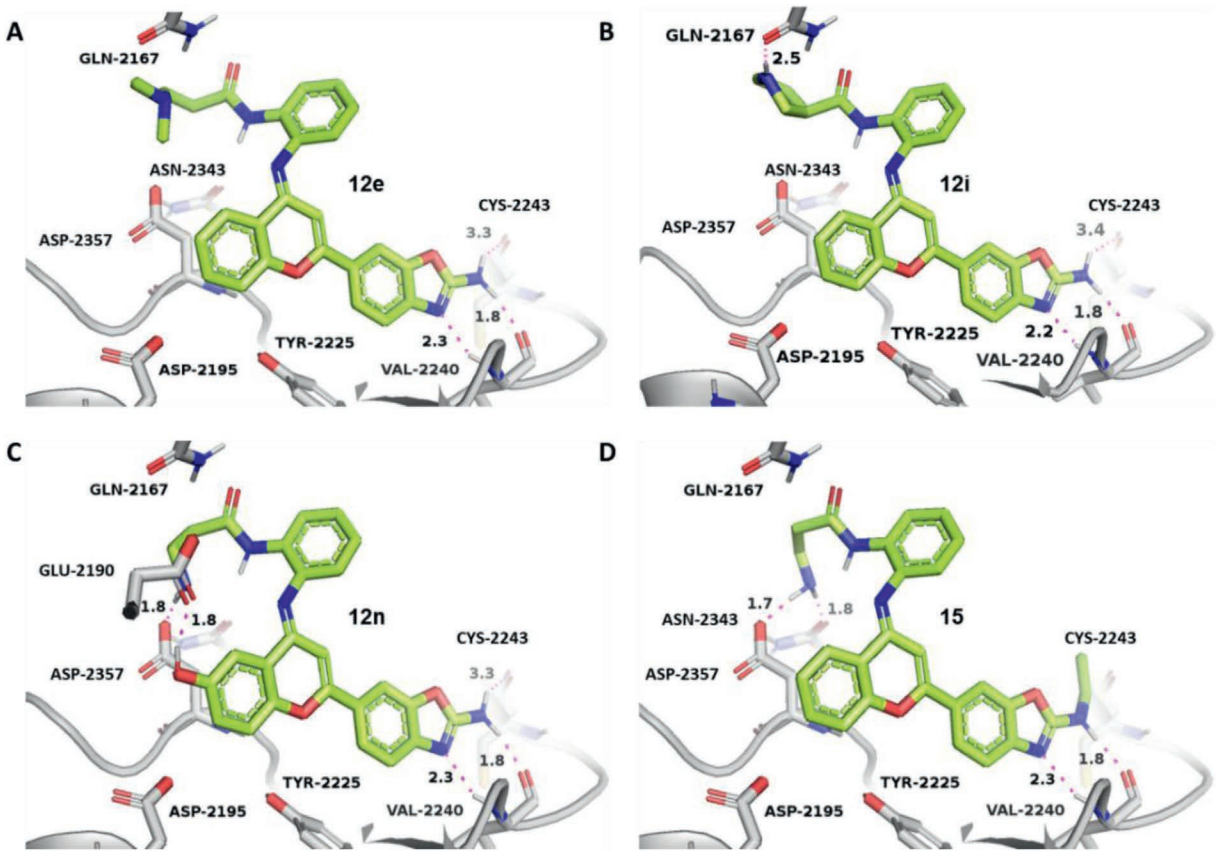

Figure 5 Binding modes of **12e** (A), **12i** (B), **12n** (C), and **15** (D) with mTOR (PDB: 4JT6).

*2.9. Induction of apoptosis by compound **MT-44***

Inducing cell apoptosis is a key therapeutic strategy in anticancer treatments[43]. The effect of **PI-103** and **MT-44** on cell apoptosis was confirmed using Annexin V-AF647/7AAD. When treated with **MT-44** at concentrations of 0.5, 1, and 2 μmol/L, the percentage of total apoptotic cells increased to 4.73%, 9.43%, and 22.23%, respectively (Fig. 10A and B). At an equivalent concentration of 2.0 μmol/L, compound **MT-44** induced a higher apoptosis rate in MDA-MB-231 cells (22.23%) than **PI-103** (4.47%). The γ-H2AX serves as a critical factor in the initiation and regulation of apoptosis[44], with its sustained presence indicating the progression of cells into the apoptotic pathway. Compound **MT-44** demonstrated a concentration-dependent effect in increasing γ-H2AX expression. Moreover, the ratio of the key apoptotic signaling proteins BAX/BCL2 also exhibited a concentration-dependent rise, with significantly elevated expression levels (Fig. 10C and D), indicating that compound **MT-44** exhibited potent inhibitory activity on tumor cells and induced cell apoptosis.

*2.10. Signaling pathway inhibitory activity of compound **MT-44***

The cellular thermal shift assay (CETSA) results further demonstrated that **MT-44** directly interacts with mTOR protein in the cellular context, inducing significant thermal stability shifts as evidenced by the altered protein aggregation profiles (Fig. 11A and B). Moreover, to elucidate the molecular mechanism by which **MT-44** inhibits tumor cell proliferation and progression, the expression levels of key proteins within the PI3K/Akt/mTOR signaling pathway were assessed through Western blot analysis. As shown in Fig. 11C, the expressions of activated p-P70S6K$^{(Thr389)}$, p-Akt$^{(Ser473)}$, and p-4EBP1$^{(Thr37/46)}$ were significantly downregulated in a concentration-dependent manner. Quantitative analysis showed that treatment with **MT-44** resulted in a more pronounced reduction in the expression levels of p-P70S6K, p-Akt, and p-4EBP1 in MDA-MB-231 cells compared with the control group (Fig. 11D).

*2.11. Compound **MT-44** induced autophagy and ROS production in MDA-MB-231 cells*

mTOR kinase plays a central role in regulating autophagy[45]. To assess further the autophagy-induced effects of **MT-44** in MDA-MB-231 cells, Western blot analysis was performed to evaluate the expression levels of autophagy-related proteins. As shown in Fig. 12A and B, the autophagy substrate P62 exhibited a concentration-dependent increase, whereas the conversion of LC3I to LC3II was more pronounced at 2 μmol/L. Similarly, immunofluorescence staining of LC3B yielded consistent results, demonstrating a concentration-dependent increase in LC3B expression (Fig. 12C and D). Notably, when the autophagy inhibitor chloroquine (CQ) was introduced, the expression level of the key autophagy-related protein LC3 II induced by **MT-44** was significantly reduced (Fig. 12E and F). These findings indicated that compound **MT-44** significantly enhanced autophagy induction in cells. As an intracellular signaling molecule, reactive oxygen species (ROS) concentration changes are closely related to apoptosis, autophagy, and other biological processe[46]. Therefore, we also examined the effect of mTOR inhibition on intracellular ROS

Table 3 Activities of the selected compounds against PI3Ks and mTOR (IC_{50}, nmol/L).[a]

Compd.	PI3Ks				mTOR
	PI3Kα	PI3Kβ	PI3Kγ	PI3Kδ	
12a	>10,000	>10,000	>10,000	>10,000	45.2 ± 8.8
12j (MT-44)	>10,000	>10,000	>10,000	>10,000	49.4 ± 17.1
PI-103	7.5 ± 0.3	14.0 ± 1.2	93.1 ± 2.0	9.3 ± 0.1	12.1 ± 0.6

[a]IC_{50} values are the mean ± SD of triplicate measurements.

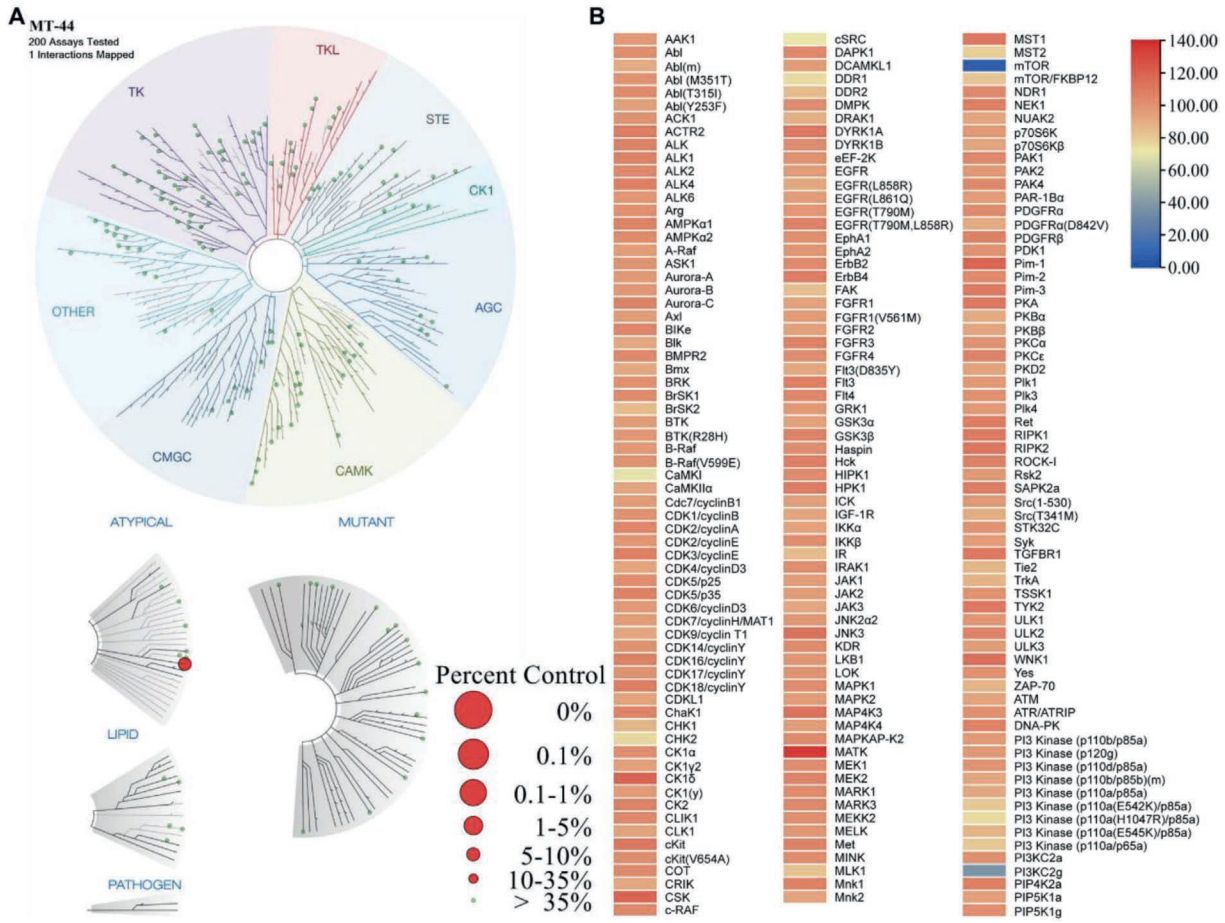

Figure 6 Kinase-specificity profiling of **MT-44** at 1.0 μmol/L concentration (Eurofins Kinase Profile platform). (A) TREEspot interaction maps of **MT-44** against 200 kinases. (B) Heat map of the %Ctrl (percent control) values of **MT-44** against various kinases. The %Ctrl values were calculated using the following formula: (test compound signal − positive control signal)/(negative control signal − positive control signal) × 100%; test compound: **MT-44**; negative control: DMSO (100% Ctrl); positive control: control compound (0% Ctrl).

levels. By FACS analysis (Fig. 12G), we found that **MT-44** treatment significantly increased ROS production in MDA-MB-231 cells, and the concentration-dependent effect of **MT-44** was particularly significant (Fig. 12H). Fluorescence imaging results (Fig. 12I) further confirmed the ROS accumulation, suggesting that mTOR inhibition may affect cell fate by inducing ROS production.

2.12. *MT-44 induced immune signaling activation in TNBC*

To elucidate further the antitumor mechanism of **MT-44** against TNBC cells, we performed an RNA-seq analysis (Fig. 13). The heat map (Fig. 13A) illustrates differential gene expression profiles in TNBC cells treated with **MT-44**. KEGG pathway analysis (Fig. 13B) showed significant enrichment of genes associated with multiple pathways, including mTOR signaling, autophagy, cell cycle regulation, p53 signaling, PD-L1 expression, and amino acid metabolism. This broad-spectrum modulation suggested that **MT-44** exerts multifaceted effects on cellular processes. Moreover, the volcano plot (Fig. 13C) demonstrated that **MT-44** treatment induced significant differential expression of genes such as *EGR1*, *TXNIP*, *DKK1*, *TIMP3*, and *TMEM156* at the mRNA level, with notable upregulation or downregulation. These genes are implicated in enhancing mTOR inhibitory activity, promoting ROS accumulation, influencing cancer metastasis, and modulating immune responses[16]. The differential expression of these genes further indicated that **MT-44** not only suppressed mTOR but also

Table 4 Antiproliferative activities of the selected compounds.

Compd.	$IC_{50} \pm SD$ (μmol/L)[a]			
	MDA-MB-231	MDA-MB-436	MCF-7	HCT-116
12a	0.3373 ± 0.0128	0.4979 ± 0.0181	0.1176 ± 0.0636	1.5086 ± 0.3606
12c	0.1043 ± 0.0033	0.5655 ± 0.0091	1.3160 ± 0.0064	0.9005 ± 0.0055
12k	0.1248 ± 0.0059	0.1123 ± 0.0623	0.2111 ± 0.0877	0.3079 ± 0.0022
12j (MT-44)	0.0665 ± 0.0015	0.1482 ± 0.0017	0.3278 ± 0.0054	0.5552 ± 0.3147
12m	>10	>10	>10	>10
12n	1.7655 ± 0.4731	NT[b]	0.5474 ± 0.6790	1.5683 ± 0.1316
12i	0.2847 ± 0.4255	NT	1.4870 ± 0.0028	313.20 ± 0.0057
PI-103	>10	>10	2.7885 ± 0.3465	>10
MLN-0128	0.1790 ± 0.2381	NT	NT	NT
Everolimus	2.2850 ± 0.0763	NT	NT	NT
Paclitaxel	3.8621 ± 0.0132	NT	NT	NT
Doxorubicin	0.0756 ± 0.2700	NT	NT	NT

[a]Data are presented as the mean values ± SD from experiments conducted in triplicate at three independent times.
[b]Not tested.

regulated other critical cellular pathways, including apoptosis and the transcription of MYC target genes (Supporting Information Fig. S1), thereby augmenting its overall therapeutic efficacy. Intriguingly, **MT-44** treatment was associated with significant enrichment of immune response-related pathways, including the RIG-I-like receptor, T cell receptor, and cAMP signaling pathways. Building on these findings, we initially investigated the effects of **MT-44** on PD-L1 and CCR1 expressions. The results indicated that **MT-44** did not change the protein levels of PD-L1 or CCR1 (Fig. 13D and E). Notably, using a TLR2-NF-κB-Luc HEK293 reporter assay, we found that **MT-44** potently activated TLR2 signaling with an EC_{50} value of 1.39 μmol/L, whereas neither the mTOR allosteric inhibitor rapamycin nor the ATP-competitive inhibitor PI-103 elicited detectable signal activation at equivalent concentrations (Fig. 13F). Moreover, **MT-44** also activated the phosphorylation of the key protein P65 in NF-κB signaling and upregulated P53 protein expression in a concentration-dependent manner, while exhibiting no detectable effect on Notch signaling (Fig. 13G and H). Subsequently, we explored the cGAS/STING signaling pathway, a convergence point for NF-κB, RIG-I-like receptors, and cAMP signaling[47,48]. As shown in Fig. 14A and B, **MT-44** induced a concentration-dependent increase in the phosphorylation of $STING^{(Ser366)}$, $TBK^{(Ser172)}$, and $IRF3^{(Ser366)}$, thereby activating the cGAS/STING pathway. The immunogenic cell death (ICD) induced by **MT-44** was further validated in MDA-MB-231 cells, where the expression levels of key ICD markers—calreticulin (CRT) and high-mobility group box 1 (HMGB1), were significantly altered in a concentration-dependent manner (Fig. 14C−E). These comprehensive findings highlighted the potential of **MT-44** to not only target mTOR inhibition but also modulate immune activation.

2.13. Machine learning model predictions

Based on the evaluation metrics (SE, SP, MCC, ACC, AUC, F1, BA) of six models for binary classification of mTOR-active compounds based on molecular fingerprints (Supporting Information Table S3), the XGBoost and RF models with better predictive performance were selected to predict the scores of compounds **MT-1**, **MT-44**, and **12n.** As shown in Table 5, the predicted scores of compounds **MT-44** (0.9375, 0.8374) and **12n** (0.9463, 0.8390) were higher than those of **MT-1** (0.5067, 0.6275) in XGBoost and RF models, which is consistent with our experimental results.

2.14. Molecular docking and molecular dynamics simulation

To investigate the potential binding modes and selectivity profiles over PI3Ks, we compared the binding postures of **MT-44** in PI3Kα and mTOR proteins by molecular docking. As shown in Fig. 15A, **MT-44** could not form a key hydrogen bond interaction with residue Val of PI3Ks that was deemed to be crucial for their kinase inhibition[49]. Fig. 15B details the binding modes of **MT-44** with mTOR, which were similar to those of compound **12a** (Fig. 4C). The results further validated the kinase selectivity of **MT-44** for mTOR. We further performed the 100 ns molecular dynamics simulations for **PI-103** and **MT-44** with PI3Kα (PDB: 4L23) and mTOR (PDB: 4JT6) complexes, respectively, using Amber 16, and identified the key residues for binding interaction. Fig. 15C shows the RMSD plots of compounds **PI-103** and **MT-44** with PI3Kα and mTOR, respectively, and the results indicate that the simulated systems were well equilibrated.

The binding free energies of **PI-103** and **MT-44** with PI3Kα and mTOR have also been calculated using MM-GBSA methods. As shown in Table 6, the ΔG values for **PI-103**-PI3Kα, **MT-44**-PI3Kα, **PI-103**-mTOR, and **MT-44**-mTOR were −43.49, −32.49, −43.26, and −40.19 kcal/mol, respectively. Hydrogen bond interactions of **PI-103** and **MT-44** with PI3Kα and mTOR were analyzed using the CPPTRAJ program in Amber 16, and the corresponding data are listed in Supporting Information Table S4, which showed that the hydrogen bond appearance time accounted for above 10% in the entire simulation process. The **MT-44**-mTOR complex formed moderate to strong hydrogen bond interactions with residues Cys-2243, Asp-2357, Asn-2343, and Val-2240, which were consistent with our previous predictions. The key residue-free energy decomposition calculation results are shown in Fig. 16A and B; Val-2240, Cys-2243, Asp-2357, and Asn-2343 were the key residues in the **MT-44**−mTOR complex, and the contribution of residue Val-851 to **MT-44** was significantly lower than that to **PI-103** in the PI3Kα complex. Furthermore, alanine scanning mutagenesis was also employed to investigate the influence of key residues on the binding free energy of the **MT-44**−mTOR complex (Fig. 16C). When residues Val-2240, Cys-2243, Asp-2357, and Asn-2343 of mTOR were

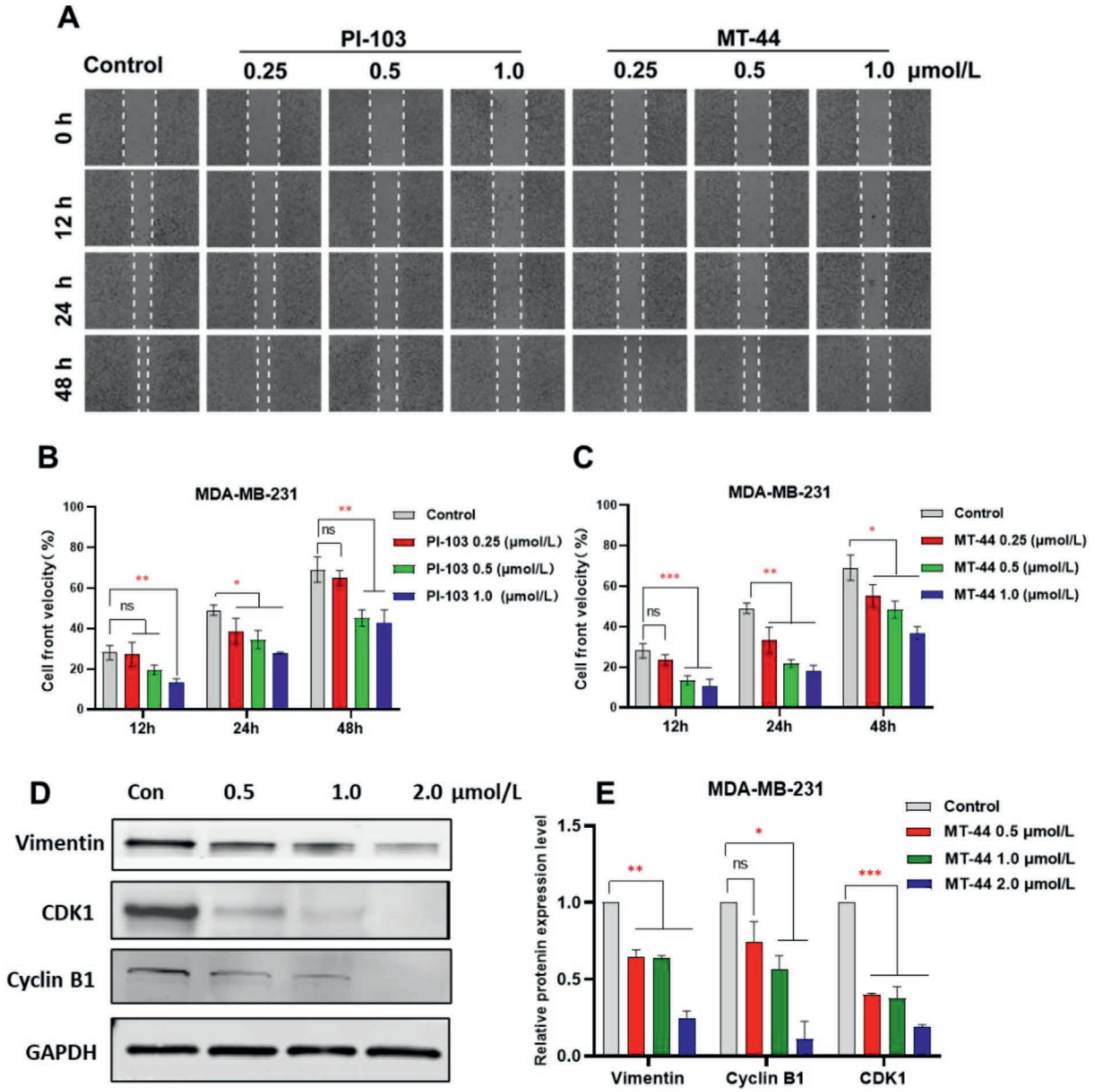

Figure 7 Anti-migration effects of compounds **PI-103** and **MT-44** on MDA-MB-231 cells. (A) MDA-MB-231 cells were treated with **PI-103** and **MT-44** (0.25, 0.5, and 1.0 μmol/L). (B, C) Quantitative analysis of cell migration ability. (D) Western blot analysis of compound **MT-44** on protein expression related to cell proliferation and cycle progress. (E) Quantitative analysis of Western blot analysis. Data are shown as mean ± SD ($n = 3$). *$P < 0.05$, **$P < 0.01$, ***$P < 0.001$. ns, not significant.

mutated to alanine, the binding free energy fluctuated significantly, confirming that these residues were crucial for protein−ligand binding. In addition, the molecular dynamics simulations of compounds **4a**, **5a**, **5e**, **12a, 15**, **12e**, **12n**, and **12i** were investigated, and the results indicated that the binding free energy with mTOR agreed well with the experimental results (Supporting Information Table S5 and Fig. S2).

2.15. Metabolic stability studies and cytochrome P450 (CYP) enzyme inhibition

Good metabolic stability is of great importance for the *in vivo* pharmacological evaluation of candidates. The *in vitro* metabolic stability profiles of compound **MT-44** were investigated using artificial gastrointestinal fluids, Sprague−Dawley (SD) rat plasma, and liver microsomes. The results showed that **MT-44** displayed excellent metabolic stability profiles in the above incubated conditions (Fig. 17A−C). Furthermore, the metabolite analysis of **MT-44** in human liver microsomes has also been performed, and the results indicated that the deamidation of the side chain (**I**) and hydrolysis of imine (**II**) structural motifs were the predominant metabolites (Fig. 17D). In addition, to avoid potential drug-drug interactions, the CYP enzyme inhibition of compounds **12a** and **MT-44** was investigated. Table 7 shows that **12a** exhibited potent inhibition on isoenzymes 2C9, 2C19, 2D6, and 3A4, with an inhibitory IC_{50} value below 10 μmol/L. Notably, compound **MT-44** showed no obvious inhibition on various isoenzymes, indicating a high safety profile.

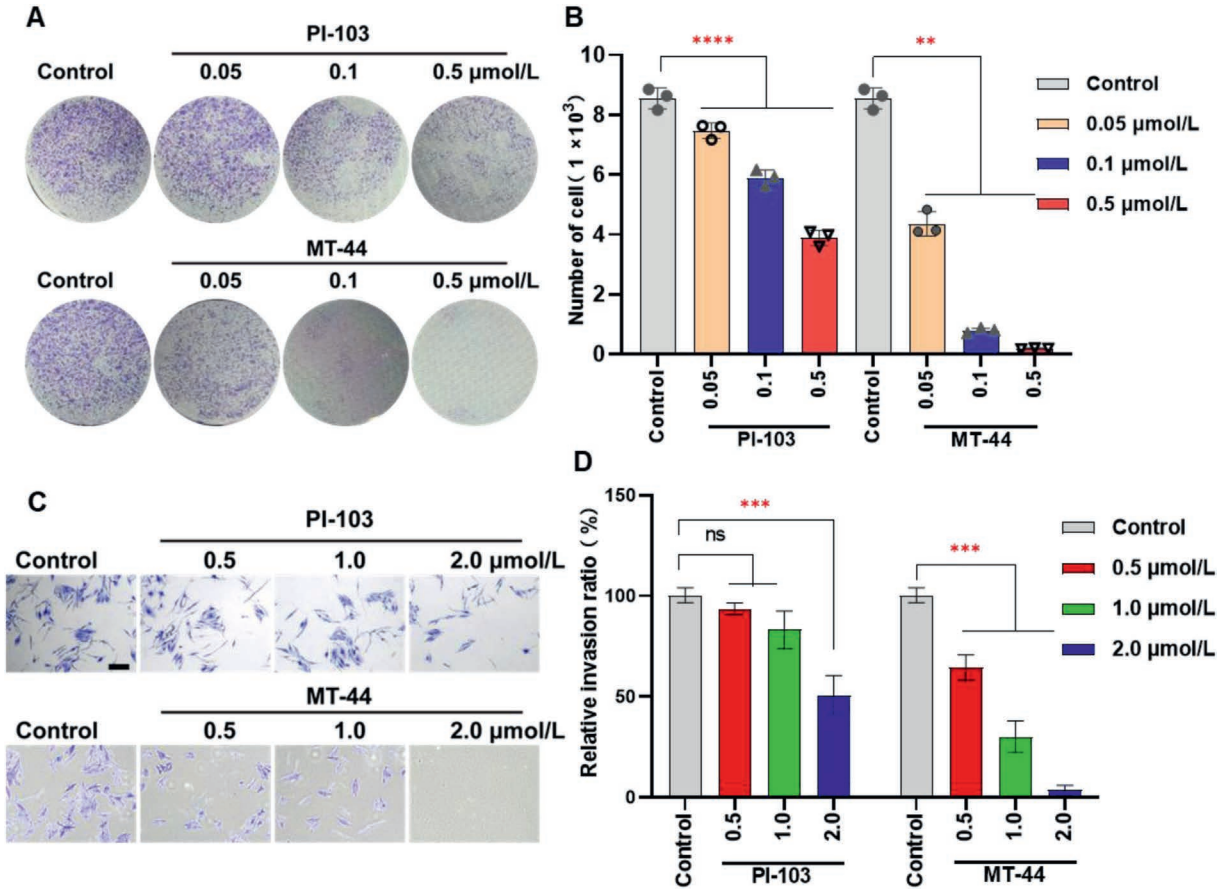

Figure 8 Colony formation and invasion inhibitory effects of compounds **PI-103** and **MT-44**. (A) MDA-MB-231 cells were treated with different concentrations of compounds **PI-103** and **MT-44** (0.05, 0.1, and 0.5 μmol/L) and stained with Crystal Violet to determine their colony-forming ability. (B) Quantitative analysis of the inhibitory effects of **PI-103** and **MT-44** on the proliferation of MDA-MB-231 cells. (C) Transwell assay in MDA-MB-231 to test the invasion ability of cancer cells. Scale bar = 100 μm (D) Quantitative analysis of the inhibitory effects of **PI-103** and **MT-44** on the invasion of MDA-MB-231 cells. Data are shown as mean ± SD ($n \geq 3$). *$P < 0.05$, **$P < 0.01$, ***$P < 0.001$, ****$P < 0.0001$. ns, not significant.

2.16. *Pharmacokinetic assay of **MT-44** in SD rats*

Pharmacokinetic (PK) parameters are an important basis for evaluating the *in vivo* pharmacodynamics of candidates. To investigate further the PK features of the optimal compound **MT-44**, SD rats were treated with **MT-44** *via* intragastric and intravenous (i.v.) administrations at doses of 20 mg/kg and 5 mg/kg, respectively. Table 8 shows that **MT-44** revealed a desirable plasma exposure and moderate, comparable mean residence time (MRT) values under i.v. administration, and long metabolic half-life and low clearance values in both modes of administration. Unexpectedly, an extremely low oral bioavailability (4.75%) was noticed, which indicated that i.v. administration was more suitable for **MT-44** *in vivo* pharmacodynamics evaluation.

2.17. *In vivo anticancer effects of **MT-44***

Given that compound **MT-44** demonstrated excellent anti-tumor effects *in vitro*, we further evaluated its *in vivo* activity. As shown in Fig. 18A−E, compared with **PI-103**, **MT-44** exhibited significant *in vivo* anti-tumor efficacy, effectively inhibiting tumor growth and weight, and demonstrating a dose-dependent trend. In addition, when **MT-44** was combined with the first-line anti-TNBC chemotherapeutic agent Doxorubicin (Doxo.), the anti-tumor effect was markedly enhanced. Specifically, the tumor growth inhibition rate (TGI) of the **MT-44** (10 mg/kg) group was 38.64%, whereas that of the **MT-44** (20 mg/kg) group was 72.73% (Table 9). The combination of **MT-44** (10 mg/kg) and Doxo., achieved a TGI of 95.45% with the average tumor volume in this group being only 29.66 ± 10.80 mm^3, significantly lower than the control group's 421.80 ± 136.31 mm^3. Subsequently, we have also assessed the biological safety and toxicity of **MT-44**. As illustrated in Fig. 18D, the body weight of mice increased after drug treatment, whereas no significant difference among the groups was noticed. Major organs were stained with hematoxylin and eosin (H&E) to assess the toxicity of **MT-44**. As shown in Fig. 18F, no significant toxicity was observed in the pathological tissues of the heart, liver, spleen, lung, and kidney in the **MT-44**, **PI-103**, and Doxo., groups compared with the control group, indicating that **MT-44** exhibited good biological safety.

To investigate the *in vivo* inhibitory effects of **MT-44** on the mTOR signaling pathway, we analyzed the expression of key mTOR-related proteins in xenograft tumor tissues. Compared with the control group, the phosphorylation levels of downstream markers, including P70S6K, 4EBP1, and AKT, were significantly reduced in the **MT-44**-treated groups (Fig. 18G and H). These

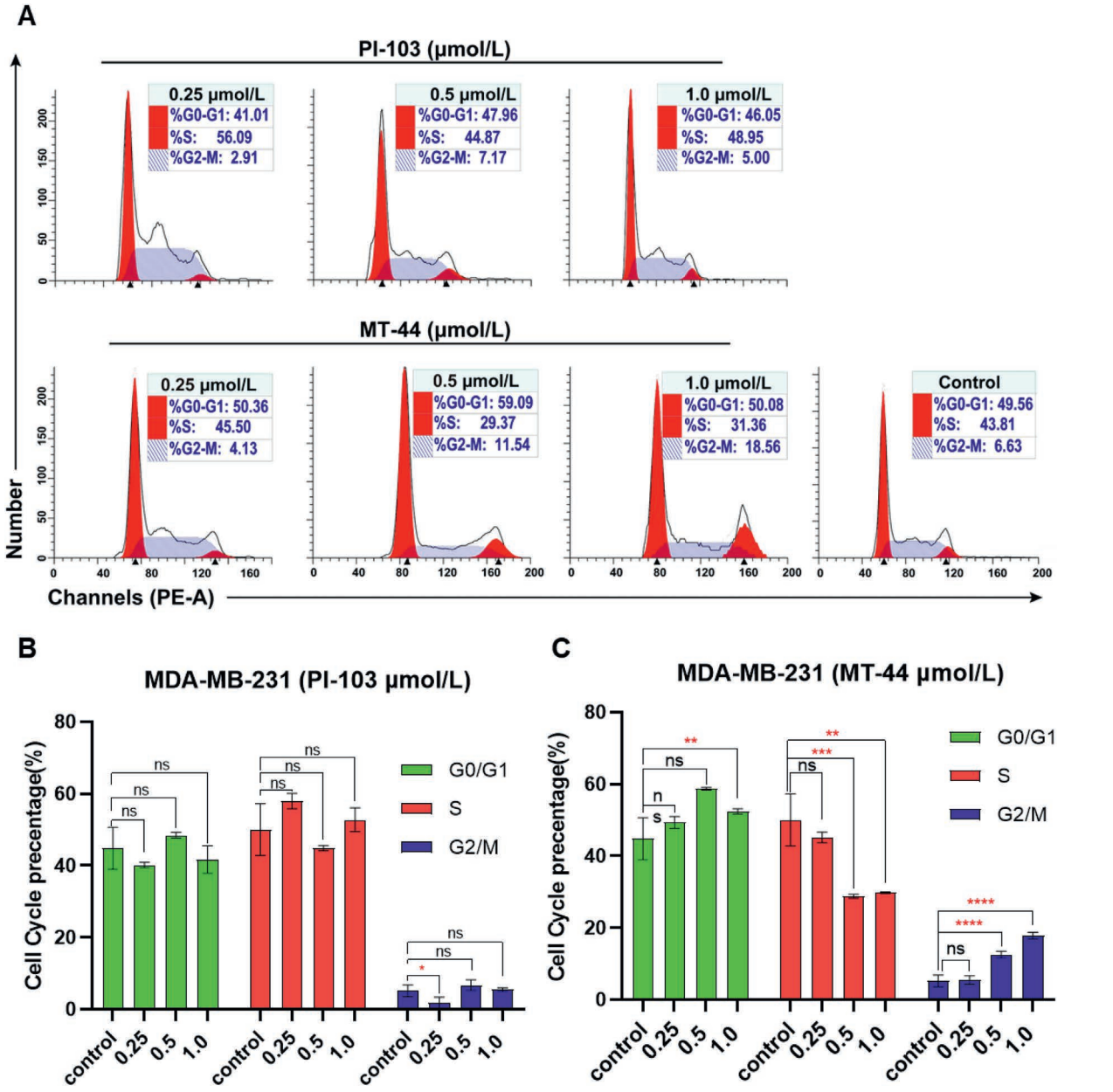

Figure 9 Compounds **PI-103** and **MT-44** induced cell cycle arrest in the G2/M phase of MDA-MB-231 cells. (A) Flow cytometry analysis of MDA-MB-231 cells treated with various concentrations of compound **PI-103** (0.25, 0.5, and 1 μmol/L) and **MT-44** (0.25, 0.5, and 1 μmol/L) for 48 h. Compound **MT-44** induced MDA-MB-231 cell cycle arrest in a concentration-dependent manner. (B) The quantified analysis of compound **PI-103**. (C) The quantified analysis of compound **MT-44**-induced cell cycle arrest in the G2/M phase of MDA-MB-231 cells. Data are shown as mean ± SD ($n \geq 3$). *$P < 0.05$, **$P < 0.01$, ***$P < 0.001$, ****$P < 0.0001$. ns, not significant.

findings indicated that **MT-44** potently suppressed the mTOR signaling pathway *in vivo*, which was consistent with the results previously observed in the *in vitro* evaluation. Furthermore, in the same xenograft tumor tissues, **MT-44** treatment markedly increased the phosphorylation levels of STING and IRF3, suggesting robust activation of the cGAS/STING signaling pathway (Fig. 18I). This observation corroborated our *in vitro* data (Fig. 13F) and highlighted **MT-44**'s dual roles in modulating both tumor-intrinsic and immune-related pathways within the tumor microenvironment. In addition, **MT-44** significantly downregulated the expression of Ki67, a well-established marker of cell proliferation, while upregulating the expression of LC3B, a critical autophagy-related protein, in the tumor tissues (Fig. 19A). These alterations underscored the anti-tumor efficacy of **MT-44**, which appeared to stem from its ability to inhibit tumor cell proliferation directly and promote autophagy. Given that **MT-44** consistently inhibited mTOR signaling and activated the cGAS/STING pathway both *in vitro* and *in vivo*, we further explored its effects on immune cell infiltration within the tumor microenvironment. Immunofluorescent analysis showed that **MT-44** treatment significantly increased the infiltration of CD56-positive natural killer cells, while concurrently reducing the presence of FOXP3-positive regulatory T cells and F4/80-positive tumor-associated macrophages (Fig. 19B). Collectively, these findings

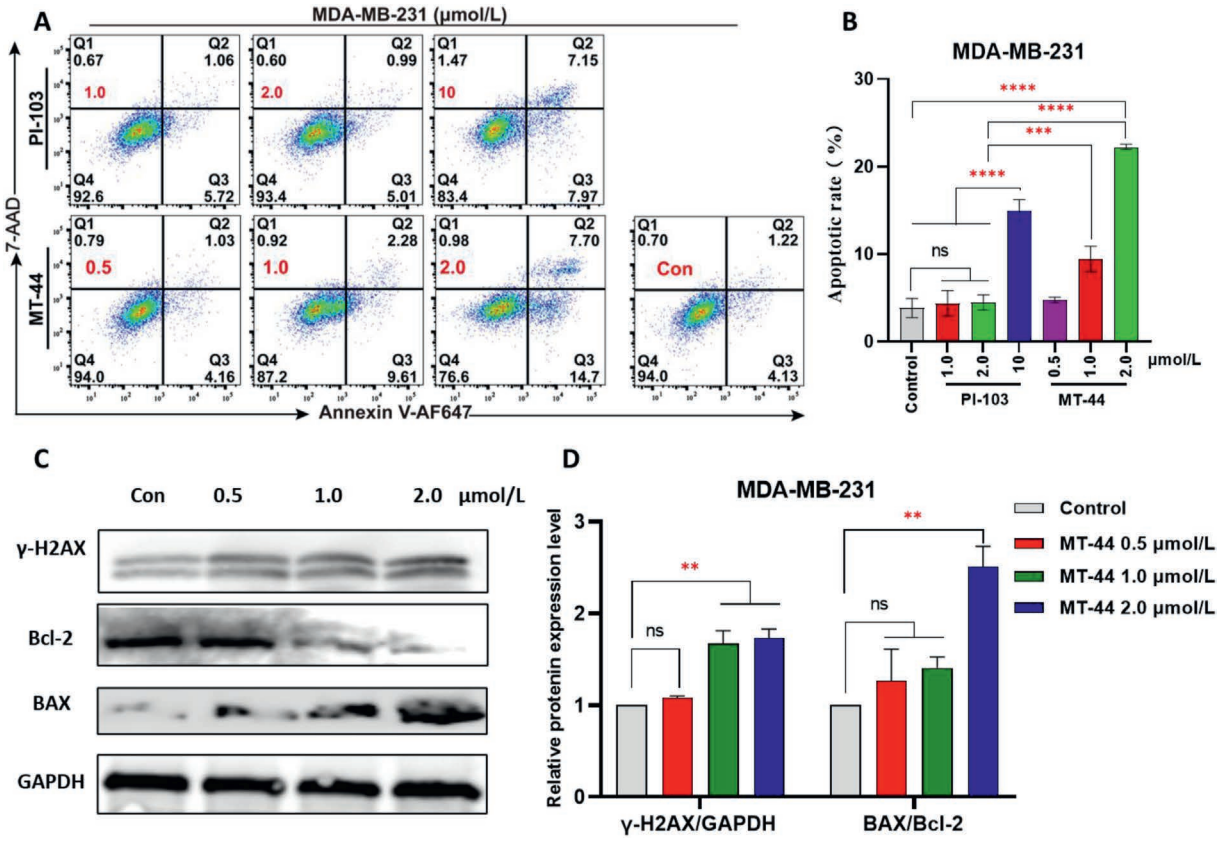

Figure 10 The effects of **PI-103** and **MT-44** on cell apoptosis in MDA-MB-231 cells. (A) MDA-MB-231 cells treated with different concentrations of **PI-103** (1.0, 2.0 and 10.0 μmol/L) and **MT-44** (0.5, 1, and 2 μmol/L) for 24 h were harvested and then stained for apoptosis analysis. (B) Quantitative analysis of apoptosis. (C) Western blot analysis of compound **MT-44** on protein expression related to cell apoptosis. (D) Quantitative analysis of Western blot analysis. Data are shown as mean ± SD ($n \geq 3$). *$P < 0.05$, **$P < 0.01$, ***$P < 0.001$, ****$P < 0.0001$. ns, not significant.

demonstrated that the novel mTOR inhibitor **MT-44** effectively suppressed mTOR signaling while simultaneously activating the cGAS/STING pathway, thereby enhancing immune cell infiltration and exhibiting robust anti-tumor efficacy.

3. Conclusions

TNBC remains one of the most formidable subtypes of breast cancer, characterized by its high metastatic potential, propensity for recurrence, and absence of targeted therapeutic agents. The aberrant activation of the mTOR signaling pathway is closely related to survival and the progression of TNBC. Considering the high impression of immune-related proteins, the combination of mTOR-targeted inhibition and immunoregulation represents a promising therapeutic strategy against TNBC. In this study, we developed a highly selective and potent mTOR inhibitor, **MT-44**, using an AIDD and SBDD integrated drug design strategy, which showed nanomolar-level antiproliferative activity on the TNBC cell line MDA-MB-231. The potential anti-tumor mechanism of **MT-44** was investigated on MDA-MB-231 cells by migration and invasion, colony formation, cell cycle arrest, apoptosis, autophagy, and ROS production assays. RNA-seq analysis showed that **MT-44** indicated significant suppression of the PI3K/Akt/mTOR and immune response-related pathways, which were preliminarily verified using Western blot and immunofluorescence analysis, both *in vitro* and *in vivo* assays. Notably, **MT-44** exerted potent TLR2 agonistic activity, which was different from other allosteric and ATP-competitive mTOR inhibitors, and it could induce MDA-MB-231 cells' immunogenic cell death. **MT-44** exhibits good metabolic stability and safety profiles, and exerts robust anti-tumor efficacy in an MDA-MB-231 xenograft tumor model with a TGI value of 72.73% under 20 mg/kg i.v. administration (Q3D), and a tumor regression trend was noticed with the combination administration of **MT-44** with the first-line anti-TNBC agent Doxorubicin. Nonetheless, the oral pharmacokinetic parameters of **MT-44** were undesirable, and a relatively low bioavailability was obtained, which provided a new direction for our further structural modification. In addition, the accurate molecular regulatory mechanism of **MT-44** on anti-tumor immunity needs to be further confirmed.

Collectively, our findings provided a novel chromone-based derivative **MT-44** as a highly selective and potent mTOR inhibitor for the potential treatment of TNBC, which exerted robust anti-tumor efficacy *via* mTOR protein-targeted inhibition and triggering of anti-tumor immunity.

4. Experimental

4.1. Chemistry and general methods

All the solvents and reagents were from commercial sources and used without further purification. All the compounds were characterized by their ^{1}H and ^{13}C NMR on a Bruker Avance NEO 400/

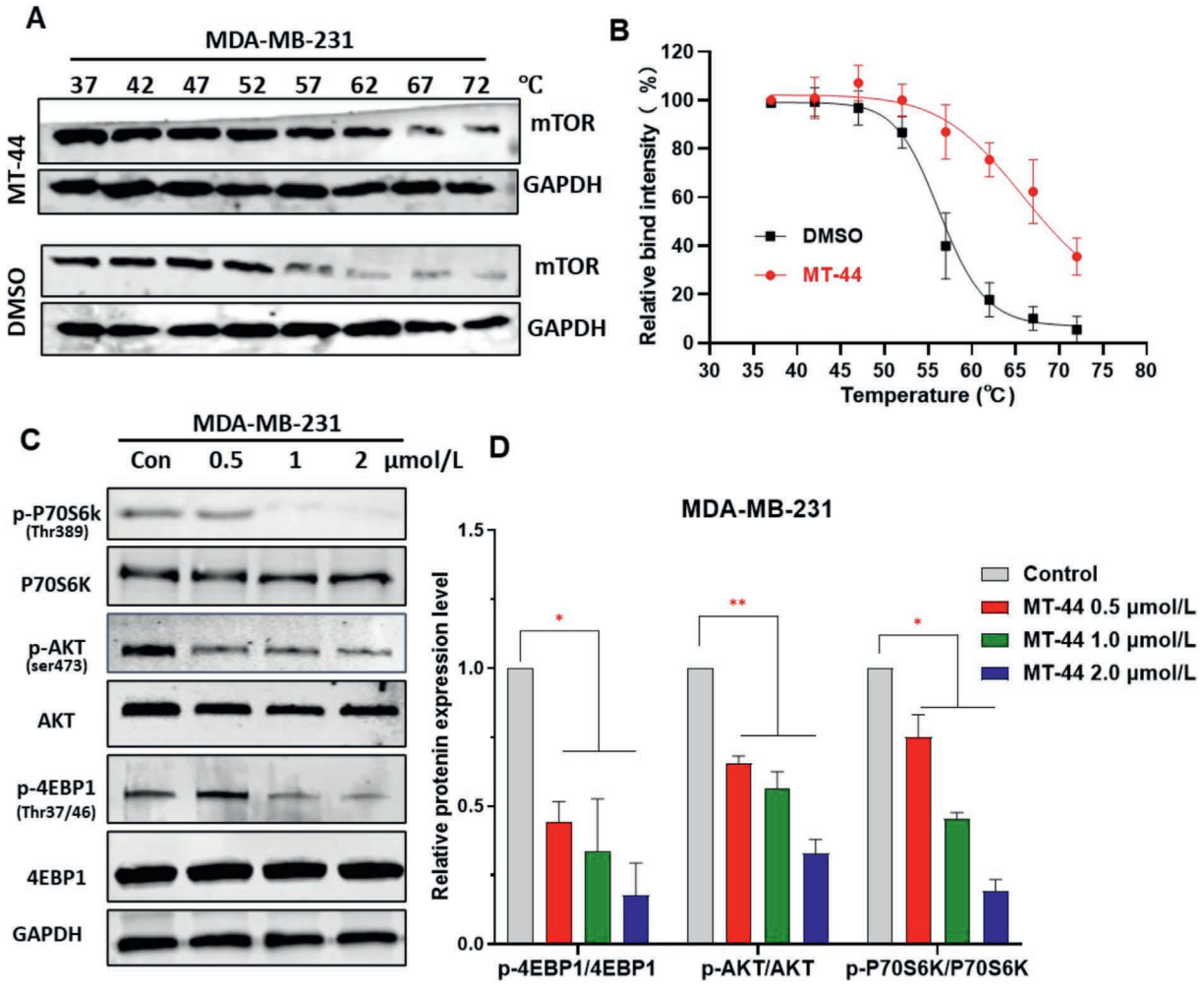

Figure 11 Western blot assay of the selected compound **MT-44** in MDA-MB-231 cells. (A) Western blot analysis, and (B) quantitative analysis of mTOR from CETSA with MT-44 in MDA-MB-231 cells. (C) MDA-MB-231 cells were treated with **MT-44** at concentrations of 0.5, 1, and 2 μmol/L for 24 h. Following treatment, cells were harvested for analysis of the PI3K/Akt/mTOR signaling pathway and its downstream effectors using Western blotting. (D) Quantitative analysis of Western blot analysis. Data are expressed as mean ± SD ($n \geq 3$) *$P < 0.05$, **$P < 0.01$.

600 MHz NMR spectrometer (Bruker BioSpin GmbH, Rheinstetten, Germany). Data for ^{1}H NMR spectra are reported in terms of chemical shift (δ, ppm), coupling constant (Hz), integration, and multiplicity (s = singlet, d = doublet, t = triplet, q = quartet, and m = multiplet). ^{13}C NMR spectral data are reported in terms of chemical shift (relative to the central line of the chloroform signal (δ = 77.06 ppm)) and multiplicity. High resolution ESI was performed on Waters G2-XS Q-Tof mass spectrometer (Waters Corporation, Milford, USA). All compounds are >95% pure by high-performance liquid chromatography (HPLC, Waters 2695) equipped with a Waters C18 column (250 mm × 4.6 mm, 5 μm, CHP-C18-A25046), using MeOH/H_2O (0.1% Et_3N) = 90/10 as the mobile phase conditions with a flow rate of 0.5 mL/min. More information regarding the chemical synthesis and structural characterization was provided in Supporting Information

4.2. *Shape screening*

Shape screening approaches have demonstrated the ability to identify hits in virtual screening and are commonly used to perform screening libraries of tens of millions of compounds[50]. We perform a shape screening *via* the Shape Screening workflow of Schrödinger. The Pharmacophore Types, as volume scoring, wrote out at most 1 alignment per ligand and filtered out conformers with similarity below 0.8. The other parameters remain at the default settings. Conformers with similarity below 0.8 compared with PI-103 were filtered out, and then the remaining ligands were selected for further study.

4.3. *Data collection, preparation and model construction*

4.3.1. *Data collection and preparation*

All compound information was collected from the ChEMBL database by querying "mTOR," yielding a total of 4545 unique molecules. To focus on direct mTOR binders, we first excluded any compound annotated with rapamycin-binding-site-related terms ("FKBP12," "FKBP," "Rapamycin," "FK506," "FRB domain," "FKBP-rapamycin complex," "FRAP," "FRAP1," "Binding to FKBP," "FKBP inhibitor," "FKBP-ligand interaction," "FKBP-binding," and "RAR"). We then retained only those entries reporting quantitative bioactivity values (IC_{50},

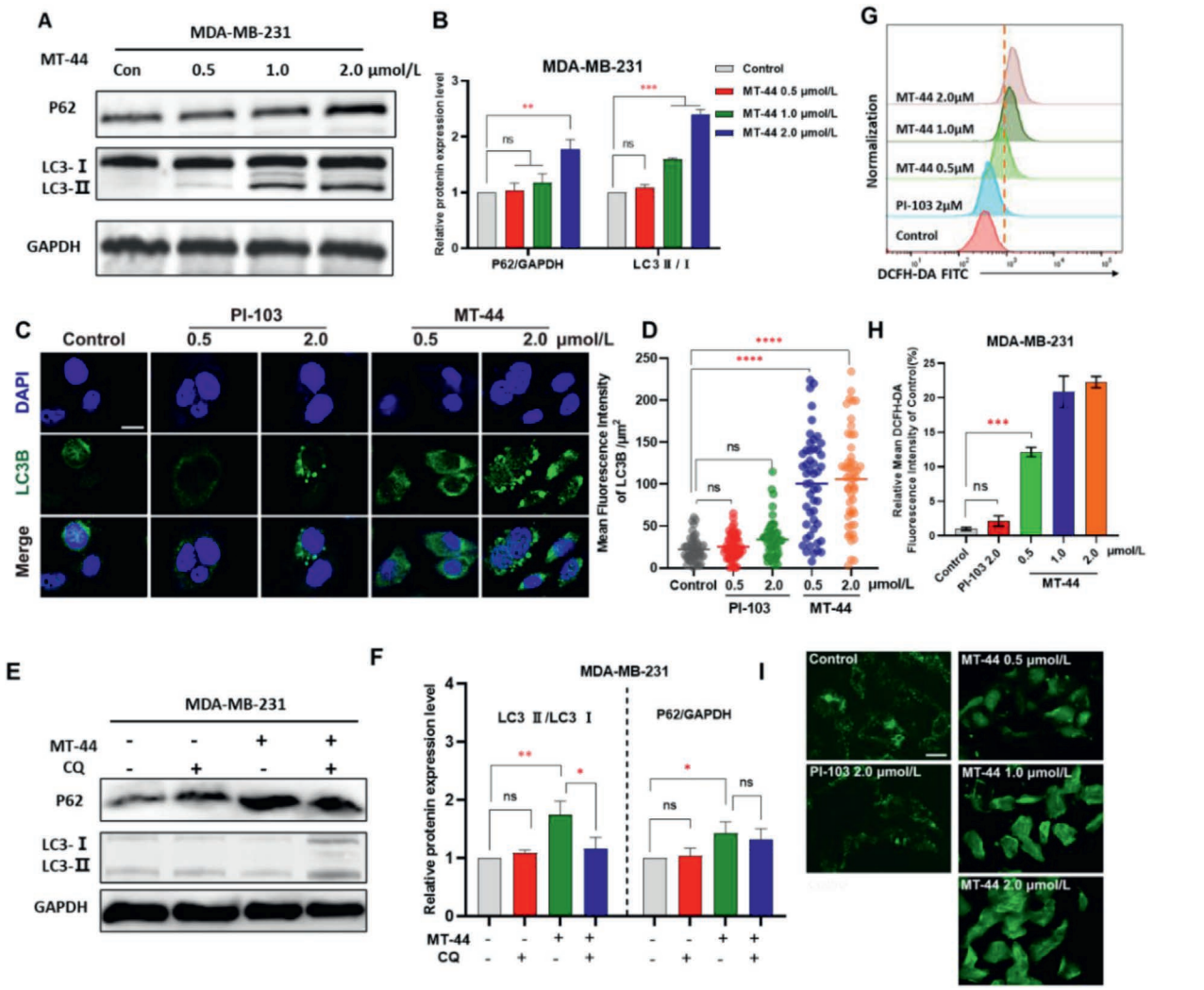

Figure 12 Compounds **PI-103** and **MT-44** induced autophagy in MDA-MB-231 cells. (A) Western blot analysis of protein expression related to autophagy in MDA-MB-231 cells induced by **MT-44** at different concentrations (0.5, 1, and 2 μmol/L) for 24 h. (B) Quantification of Western blotting analysis is shown. (C) Immunofluorescence staining of LC3B and DAPI in MDA-MB-231. Cells were treated with **PI-103** (0.5 and 2.0 μmol/L) or **MT-44** (0.5 and 2.0 μmol/L) for 24 h (scale bar = 20 μm). (D) Quantitative analysis of mean fluorescence intensity. (E) The expression level of LC3 II transformation induced by **MT-44** in MDA-MB-231 cells with or without chloroquine (CQ, 5 μmol/L, for 4 h). (F) Quantitative analysis of Western blot analysis. (G) ROS levels of DCFH-DA in MDA-MB-231 cells treated with compounds **PI-103** (2.0 μmol/L) and **MT-44** (0.5, 1.0, and 2.0 μmol/L) were detected using FACS. (H) Quantification of the percentage of ROS-positive cells in different groups. (I) Fluorescence images of MDA-MB-231 cells incubated with compounds **PI-103** and **MT-44** were then stained with the ROS fluorescence probe DCFH-DA (scale bar = 20 μm). Data are expressed as mean ± SD ($n \geq 3$). *$P < 0.05$, **$P < 0.01$, ***$P < 0.001$, ****$P < 0.0001$. ns, not significant.

EC_{50}, or AC_{50}), converted all measurements to nanomolar units, and averaged multiple records for the same compound. Applying a threshold of ≤5 μmol/L for activity classification resulted in 3986 actives and 559 inactives. To evaluate chemical diversity and ensure robust model assessment, we performed stratified splits (80% training/10% validation/10% test) across five consecutive random seeds. At the Bemis−Murcko scaffold level, 1812 unique scaffolds were observed: the single most frequent scaffold accounted for only 3.6% of the dataset, while the remaining 1795 scaffolds each comprised ≤0.5%, indicating a highly uniform distribution of core chemotypes (Supporting Information Figs. S3 and S4). Under this splitting scheme, the average scaffold-level Jaccard similarity between training and test sets was 0.2076, and the mean Tanimoto similarity based on Morgan fingerprints was 0.1490 ± 0.0861, confirming limited overlap in both skeletons and substructural features (Supporting Information Table S6).

4.3.2. Model construction

This study constructed binary classification models to distinguish active and inactive compounds targeting mTOR using five conventional machine learning algorithms (Random Forest, Support Vector Machine, Naive Bayes, K-Nearest Neighbors, XGBoost) and one deep learning algorithm (Deep Neural Network, DNN). All models were trained using Morgan fingerprints (CircularFingerprint, size = 1024) as molecular descriptors, and data preprocessing and modeling were performed using the DeepChem framework. Random Forest (RF) was implemented

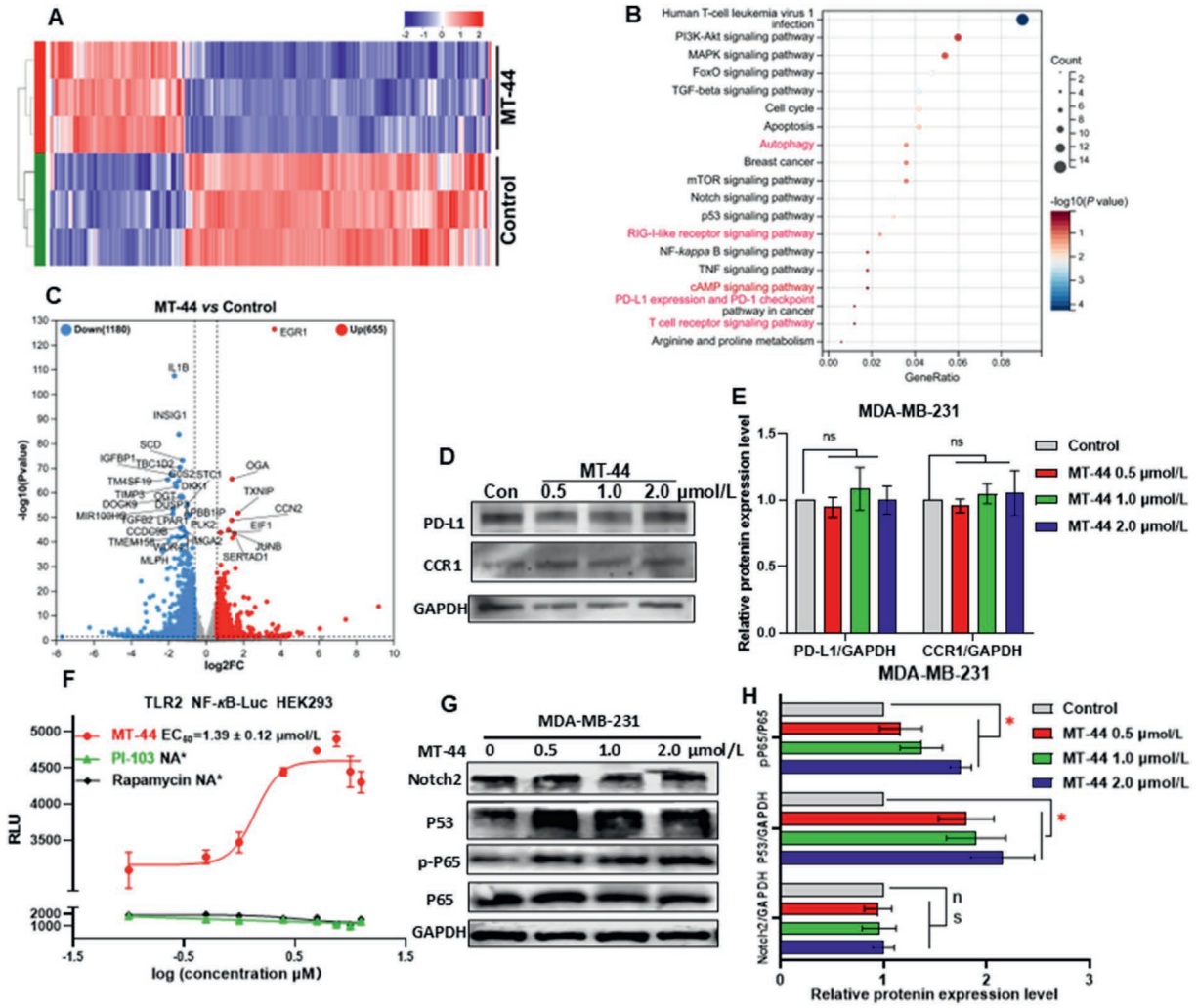

Figure 13 Gene expression profiling of MDA-MB-231 cells treated with DMSO and **MT-44** (2.0 μmol/L) for 8 h by RNA-seq. (A) Visualized heat maps of gene expression in MDA-MB-231 cells treated with the compound **MT-44** and DMSO as a control group. (B) Enrichment bubble plot illustrating KEGG pathways significantly associated with differentially expressed genes. Circle dimensions reflect gene counts per pathway, with color gradients denoting adjusted *P*-values. (C) Volcano plot displaying |log2(fold change)|>1.5 *versus* −log10(FDR) for differential expression. (D, E) Dose-dependent effects of **MT-44** (0.5-2.0 μmol/L, 24 h) on immune-related protein expression by immunoblot with densitometry. (F) The TLR2 NF-κB-Luc HEK293 cells were incubated with different concentrations of the compounds for 6 h, and then the activation degree was measured by using an enzyme reader to measure the absorbance. NA: no activating effect at the same concentration. (G, H) Western blot was used to detect the levels of changes in related signaling pathways.

using Scikit-learn, with parameters set to n_estimators = 100, max_depth = 15, and criterion = 'entropy', while other parameters were left as default. Support Vector Machine (SVM) was constructed using Scikit-learn's SVC class with an RBF kernel, C = 1.0, gamma = 'scale', and probability = True enabled. Naive Bayes (NB) used GaussianNB with the default configuration. K-Nearest Neighbors (KNN) employed KNeighborsClassifier with n_neighbors = 5, using Jaccard distance as the similarity metric. XGBoost was implemented *via* the xgboost package, with hyperparameters including: max_depth = 6, eta = 0.1, alpha = 0.5, lambda = 1, colsample_bytree = 0.8, subsample = 0.8, and n_jobs = −1. Early stopping was applied using early_stopping_rounds = 10 to prevent overfitting. The Deep Neural Network (DNN) was built using DeepChem's MultitaskClassifier, configured as a three-layer fully connected neural network (1024 → 512 → 256) with ReLU activation and dropout (rate = 0.2) for regularization. The learning rate was set to 0.001, batch size to 128, and the model was trained for 10 epochs. To ensure fair and robust evaluation, all models were trained and evaluated using five different random seeds to split the dataset into training (80%), validation (10%), and test (10%) sets. After each split, models were independently trained, and the following performance metrics were calculated: Accuracy (ACC), Sensitivity (SE), Specificity (SP), Matthews Correlation Coefficient (MCC), Area Under the ROC Curve (AUC), F1 Score, and Balanced Accuracy (BA). The final performance of each model was reported as the mean of the five experimental runs, ensuring robustness and representativeness of the results. Furthermore, we evaluated the stability and generalization of our final RF and XGB classifiers *via* five-fold cross-validation. The RF model achieved an average AUC of 0.9573 ± 0.0056, while the XGB model attained 0.9603 ± 0.0078

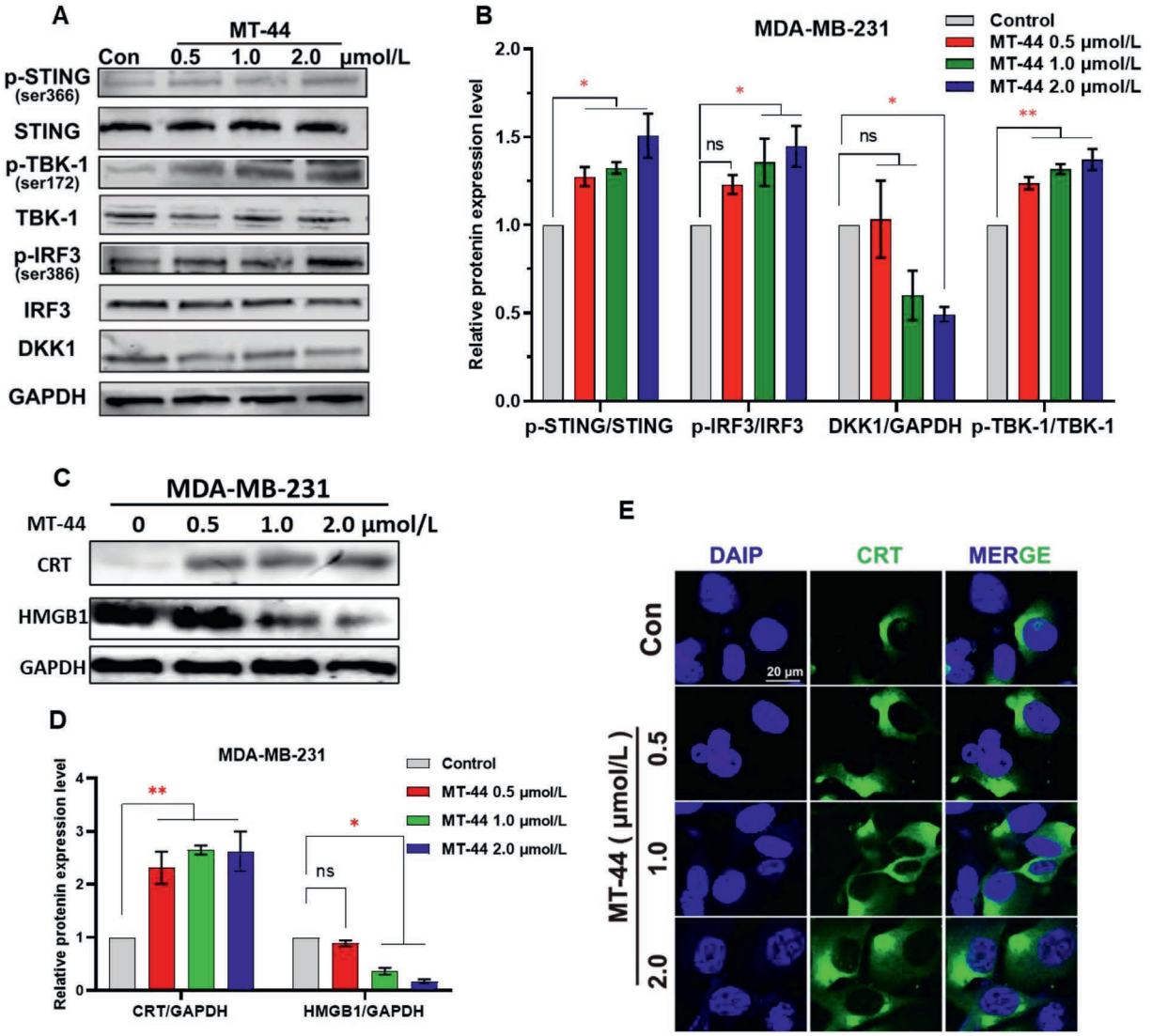

Figure 14 Preliminary exploration of the immune activation signaling pathway. (A, B) cGAS-STING signaling pathway modulation by **MT-44** (0.5−2.0 μmol/L, 24 h) was demonstrated through immunoblot and GAPDH-normalized quantification. (C, D) Western blot was used to detect and quantify the expression levels of key proteins involved in immune-mediated cell deaths. (E) Immunofluorescence staining of the immunogenic death marker protein CRT (green) and DAPI (blue) in MDA-MB-231 cells (scale bar = 20 μm). Data are expressed as mean ± SD ($n \geq 3$). *$P < 0.05$, **$P < 0.01$. ns, not significant.

(Supporting Information Table S7). These high and tightly distributed AUC values demonstrate that both models perform consistently without evidence of overfitting. After building the classification model, we used the same model parameters to construct the regression model and observe the model's prediction ability in regression. We standardized all IC_{50} measurements to the same units and applied a logarithmic transformation to train regression models, the resulting R^2 values uniformly fell below 0.8 (Supporting Information Table S8). We observed that the model performed poorly in regression prediction, and we finally adopted a categorical model for our study.

4.4. Docking and MD simulation study

The protein crystal structures of PI3Kα (PDB: 4L23) and mTOR (PDB: 4JT6) were used for docking and the MD simulation study, and the Ligand docking module in Glide (Schrödinger) was used for docking, the detailed procedures are referenced from our previous work[32]. The Amber 16 software was used for solvation, molecular dynamics (MD) simulation, and trajectory analysis. Compounds were optimized using BCC charges, the ff14SB force field, and the general amber force field (gaff2) were used for the protein and ligand, respectively, and a solvent octahedral box with a boundary 15 Å away from the complex was built, and the TIP3P water model was used to fill the entire octahedral box. The 9 Na^+ and 12 Na^+ were added to neutralize the systems of PI3Kα and mTOR, respectively. The 100 ns MD simulations were performed at 300 K with 1.0 atmospheric pressure in the NPT ensemble. The CPPTRAJ program in Amber 16 was used to analyze hydrogen bond interactions. The MMGBSA.py script was employed to calculate the binding free energy and residue free energy decomposition. For detailed steps, please refer to the molecular

Table 5 The predicted scores of compounds **MT-1**, **MT-44,** and **12n** in XGBoost and RF models.

Compd.	Prediction probability	
	RF	XGBoost
MT-1	0.6275	0.5067
MT-44	0.8374	0.9375
12n	0.8390	0.9463

dynamics simulations section in our previously published article[51].

4.5. *In vitro enzymatic assay*

The kinase inhibitory activities of the target compounds against mTOR were assessed by Shanghai ChemPartner Co., Ltd. (China). PI3K inhibition was evaluated using the ADP-Glo Luminescent Kinase Assay under reaction conditions of 50 mmol/L HEPES (pH 7.5), 100 mmol/L NaCl, 3.0 mmol/L $MgCl_2$, 2.0 mmol/L dithiothreitol (DTT), 1.0 mmol/L ethylene glycol tetraacetic acid (EGTA), and 0.03% CHAPS. mTOR inhibition was measured using the Lance Ultra assay in a buffer containing 50 mmol/LHEPES (pH 7.5), 10 mmol/L NaCl, 1.0 mmol/L EGTA, 3.0 mmol/L $MnCl_2$, 2.0 mmol/L DTT, and 0.01% Tween-20. Assays were conducted in triplicate, and IC_{50} values were determined using GraphPad Prism 8.3, with data recorded on an EnVision system. Detailed procedures can be found in our previous studies[32,34].

4.6. *Cell viability assay*

The antiproliferative activity of the target compounds was evaluated using a CCK-8 assay in seven human cancer cell lines (MDA-MB-468, MDA-MB-231, MCF-7, HCT-116, A549, H1975, and Molm-13). Cells were seeded in 96-well plates and incubated at 37 °C with 5% CO_2 for 24 h, followed by treatment with increasing concentrations of the compounds for 48 h. Subsequently, 10 μL of CCK-8 solution (2.5 mg/mL) was added to each well and incubated for 0−4 h. Absorbance was measured at 450 nm using a microplate reader (PerkinElmer, USA), and IC_{50} values were calculated using GraphPad Prism 8.3.

4.7. *Colony formation assay*

The number of MDA-MB-231 cells was 1×10^3 cells per well, and the cells were planted in a 12-well plate with DMEM culture medium (BasalMedia, Shanghai, China). Replace the medium with fresh medium containing 0.5, 1.0, or 2.0 μmol/L compounds **PI-103** and **MT-44.** After 2 weeks of culture, the cells were stained with 0.1% crystal violet solution, naturally air-dried, photographed, and statistically analyzed.

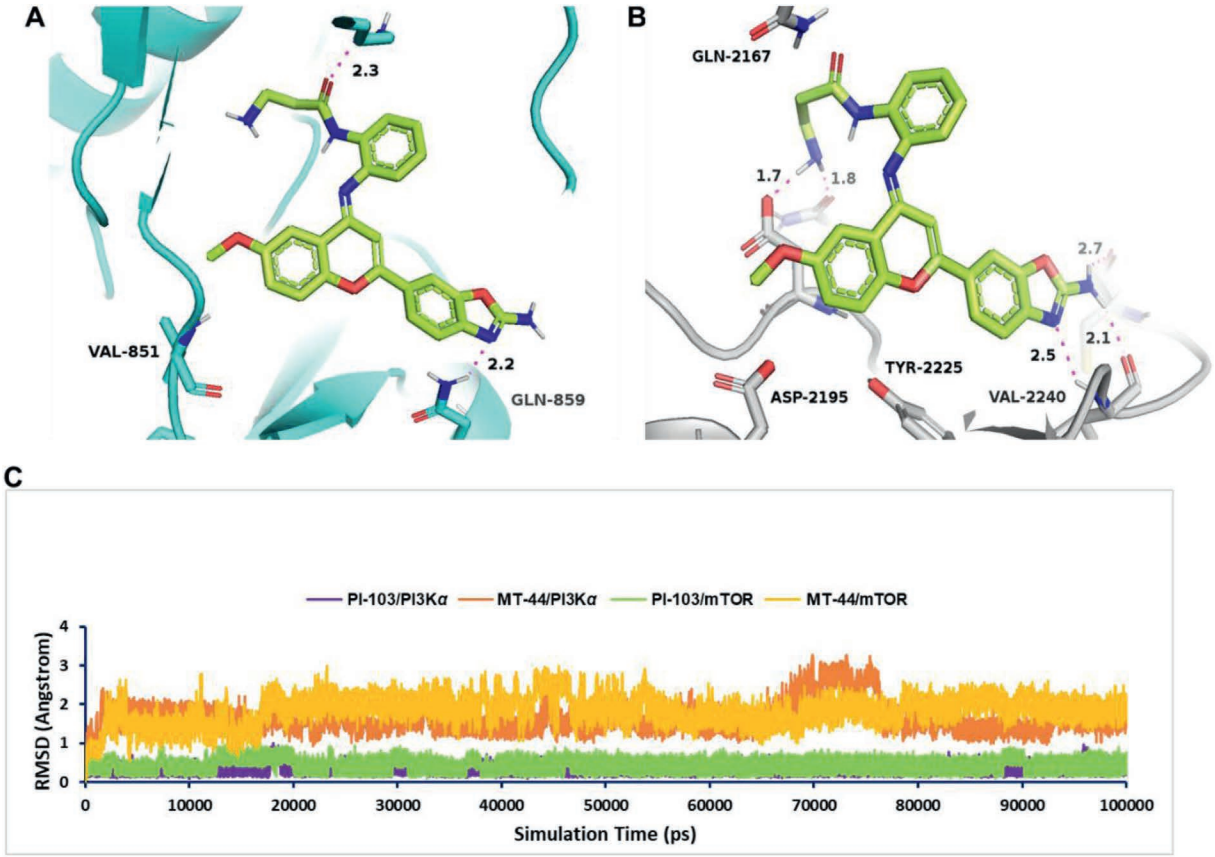

Figure 15 The binding posture prediction of **MT-44** in PI3Kα (PDB: 4L23) (A) and mTOR (PDB: 4JT6) (B) proteins. Compared with mTOR, **MT-44** cannot form a key hydrogen bond with Val-851 of PI3Kα that ensures active critical residues. (C) The RMSD plots of compounds **PI-103** and **MT-44** with PI3Kα and mTOR.

Table 6 Binding free energies of **PI-103** and **MT-44** with PI3Kα (PDB: 4L23) and mTOR (PDB: 4JT6) (kcal/mol).

Compd.	Contribution[a]						
	ΔE_{vdw}	ΔE_{ele}	ΔE_{egb}	ΔE_{esurf}	ΔG_{gas}	ΔG_{solv}	ΔG_{bind}
PI-103−PI3Kα	−39.35 ± 0.29	−25.54 ± 0.34	25.07 ± 0.25	−3.67 ± 0.01	−64.89 ± 0.30	21.40 ± 0.26	−43.49 ± 0.28
MT-44−PI3Kα	−45.17 ± 0.32	−21.79 ± 0.88	38.83 ± 0.67	−4.36 ± 0.03	−66.96 ± 0.87	34.47 ± 0.66	−32.49 ± 0.39
PI-103−mTOR	−39.12 ± 0.33	−39.81 ± 0.38	39.68 ± 0.31	−4.01 ± 0.02	−78.93 ± 0.36	35.67 ± 0.30	−43.26 ± 0.37
MT-44−mTOR	−53.39 ± 0.37	−47.24 ± 0.79	65.80 ± 0.58	−5.36 ± 0.02	−100.63 ± 0.90	60.44 ± 0.57	−40.19 ± 0.49

[a]Data are the mean ± SD of triplicate calculations.

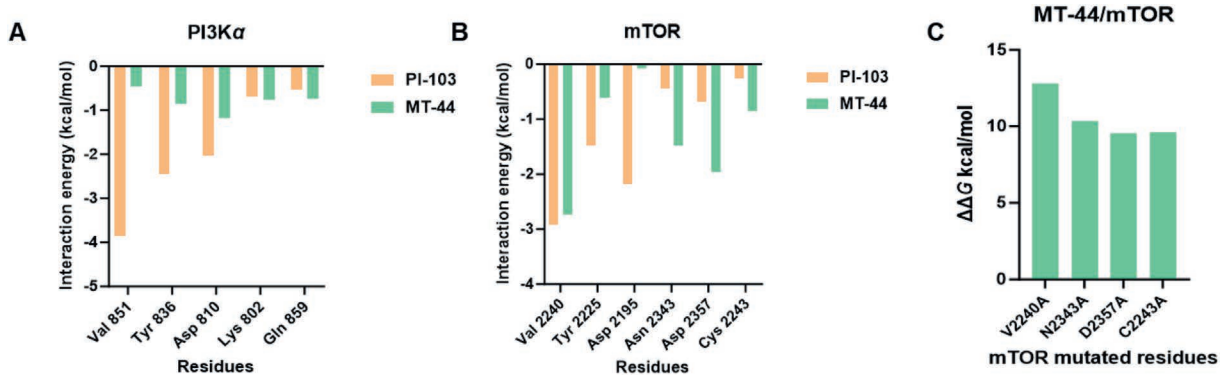

Figure 16 The key residue free energy decomposition calculation of **PI-103** and **MT-44** with (A) PI3Kα and (B) mTOR, respectively. (C) Alanine scanning mutagenesis of **MT-44**−mTOR. The 200 conformations extracted from the last 10 ns trajectories of the system were used to calculate the binding free energy. The changes in binding free energy, $\Delta\Delta G$, were calculated according to the formula ($\Delta\Delta G_{bind} = \Delta G_{bind\ mutant} - \Delta G_{bind\ wild\ type}$) between the variant and wild-type protein when the specific residue was mutated to alanine.

4.8. Cell migration assay

MDA-MB-231 cells were cultured in 12-well plates with a density of 2×10^5 cells per well for 24 h, and then cultured in complete medium containing 2% fetal bovine serum (FBS) (Gibco, Waltham, MA, USA) for 12 h after cell adhesion. Then the cells were cut with the tip of a 10 μL pipette to form wounds, and washed twice with PBS. **PI-103** and **MT-44** were then treated with three different concentrations (1.0, 1.5, and 2.0 μmol/L) and imaged under an optical microscope (Nikon, Tokyo, Japan) at 0, 12, 24, and 48 h.

4.9. Flow cytometric analysis

MDA-MB-231 cells were maintained in DMEM/F12 medium (Gibco) supplemented with 10% FBS and 1% penicillin/streptomycin at 37 °C under 5% CO_2. For experiments, cells were seeded at 2.5×10^5 cells/well in 6-well plates and treated with designated compounds for 24 h. Cells were trypsinized, washed twice with ice-cold PB, and fixed in 70% ethanol (4 °C, 2 h). Fixed cells were pelleted (300×*g*, 5 min, Eppendorf, Hamburg, Germany), resuspended in PBS containing 0.1% Triton X-100, 20 μg/mL propidium iodide, and 100 μg/mL RNase A for 30 min at 37 °C in darkness. Samples were analyzed on the FACSCanto™ II system (BD Biosciences, NJ, USA) equipped with a 488 nm laser, by detecting PI fluorescence. At least 10,000 events were obtained for each sample. The data is processed using ModFit LT 5.0 and dual identification by FSC-A and FSC-H gating. Cells were collected, washed with cold PBS, and stained using the Annexin V-AF647/7AAD Apoptosis Detection Kit (Goonie, Guangzhou, China) following the manufacturer's protocol. Briefly, cells were resuspended in 100 μL binding buffer containing 5 μL Annexin V-AF647 and 5 μL 7AAD for 15 min at 25 °C. After incubation with different concentrations of **MT-44** for 10 h, the cells were cultured with 5 μmol/L 2′,7′-dichlorodihydrofluorescein (DCFH-DA) (Medchemexpress, Shanghai, China) in serum-free medium at 37 °C for 30 min, then washed and collected. DCF fluorescence was quantified in FITC-A. Data were normalized to untreated controls and expressed as geometric mean fluorescence intensity using FlowJo v10.8.

4.10. RNA sequencing and bioinformatic analysis

Total RNA was isolated from **MT-44**-treated or untreated MDA-MB-231 cells using TRIzol reagent (Absin, Shanghai, China). RNA sequencing was performed following the protocols provided by Majorbio. Raw data processing and bioinformatic analysis were conducted *via* the freely accessible Majorbio Cloud Platform (www.majorbio.com).

4.11. Western blotting analysis

The cell lysates were dissolved in 10% SDS-PAGE under reduced conditions and then transferred to a polyvinylidene fluoride (PVDF) membrane (pore size 0.45 μm; Millipore) using a wet transfer system (200 mA, 60 min). Use 5% (*w*/*v*) skim milk powder (Bio-Rad) in tris-buffered salt water (TBS; 20 mmol/L Tris-HCl, 150 mmol/L NaCl, pH 7.4) at room temperature for 1 h. Primary antibody was incubated in TBS containing 0.05% Tween-20 (TBST) at 4 °C for 16 h. Primary antibodies used in this article include: phospho-4EBP1 rabbit mAb (Cell Signaling Technology, 2855s, Cambridge, USA), 4EBP1 (Proteintech, 60246-1-AP, Rosemont, USA), phosphor-IRF3 rabbit mAb (Huabio, ET1608-22, Hangzhou, China), Cyclin D1 rabbit mAb (Cell Signaling

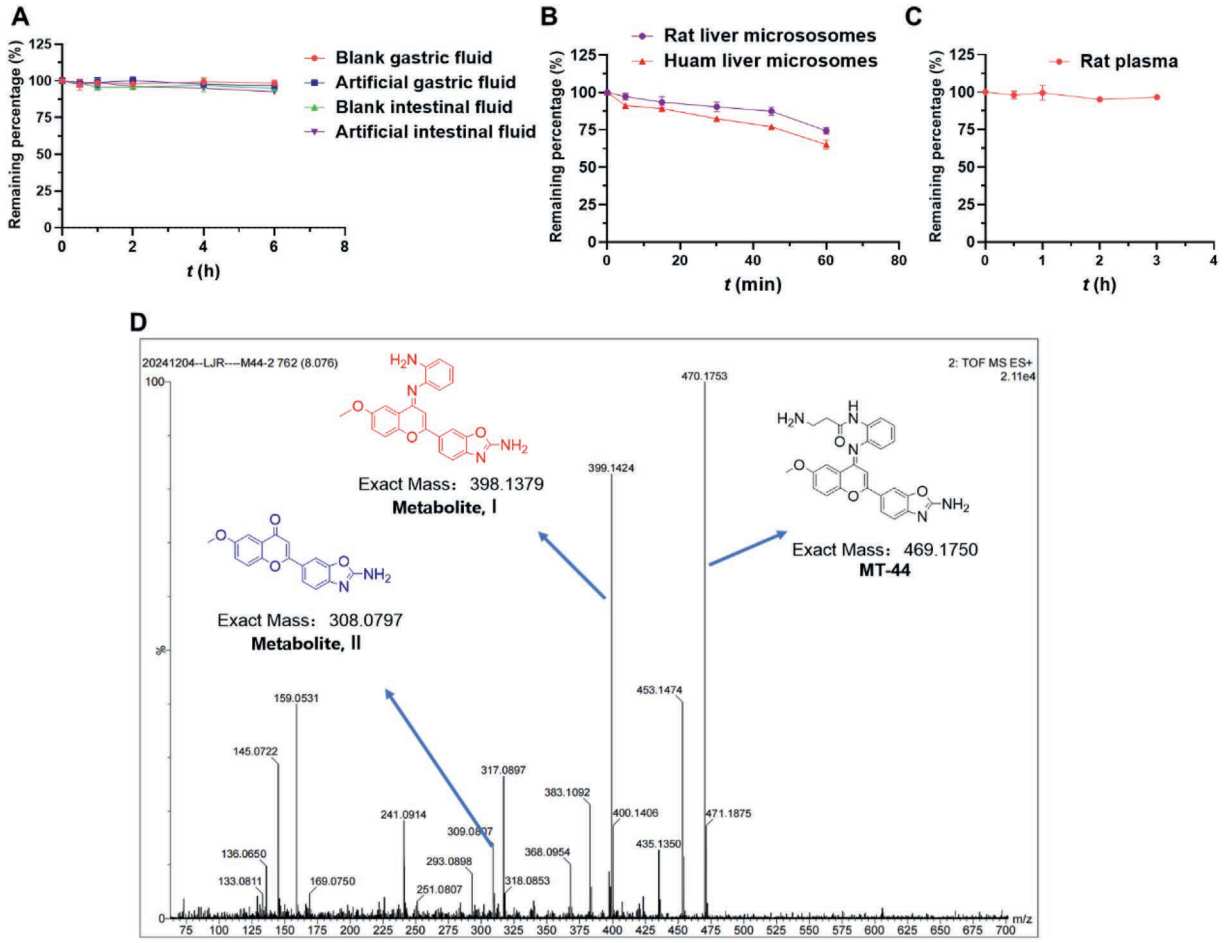

Figure 17 Metabolic stability of compound **MT-44**. (A) Artificial gastrointestinal fluids with **MT-44** ($n = 3$). (B) SD rat plasma stability ($n = 3$). (C) Liver microsome stability ($n = 3$). (D) Analysis of metabolites in human liver microsomes.

Table 7 CYP enzymes inhibition of compounds **12a** and **MT-44**.

Compd.	IC_{50} (μmol/L)				
	1A2	2C9	2C19	2D6	3A4
12a	>50	0.14	0.68	5.52	7.86
MT-44	>50	>50	>50	19.89	>50

Technology, 55506T), mTOR rabbit mAb (Cell Signaling Technology, 2983S), phospho-AKT rabbit mAb (Cell Signaling Technology, 4249T), phospho-P70S6K rabbit mAb (Proteintech, 28735-1-AP), STING rabbit mAb (STARTER, S0B0906, Hangzhou, China), CRT rabbit mAb (STARTER, S0B0474), TBK1 rabbit mAb (STARTER, S0B0449), PD-L1 rabbit mAb (Huabio, HA721176), cGAS rabbit mAb (STARTER, S0B0396), LC3B rabbit mAb (Huabio, ET1701-65), GAPDH monoclonal antibody

Table 8 Pharmacokinetic parameters of compound **MT-44** in SD rats[a] ($n = 6$).

Parameter	Unit	i.v.[b] (5 mg/kg)	i.g.[c] (20 mg/kg)
$AUC_{(0-30)}$	μg/L × h	28,750.06 ± 2461.20	5303.27 ± 514.18
$AUC_{(0-inf)}$	μg/L × h	29,902.44 ± 2360.94	5677.69 ± 501.28
$MRT_{(0-30)}$	h	2.93 ± 0.16	5.44 ± 0.20
T_{max}	h	0.05	1.40 ± 0.55
$t_{1/2}$	h	14.14 ± 3.35	13.97 ± 4.11
Cl	mL/min/kg	0.17 ± 0.01	0.75 ± 0.07
V_{ss}	L/kg	4.43 ± 0.93	15.04 ± 4.24
C_{max}	μg/L	29,237.95 ± 2081.44	1148.14 ± 174.19
F	%	–	4.75

[a]AUC: area under the plasma concentration−time curve; MRT: mean resonance time; T_{max}: peak time; $t_{1/2}$: half-life; Cl: clearance; V_{ss}: volume of distribution at steady state; C_{max}: peak concentration; F: oral bioavailability.
[b]i.v.: intravenous administration.
[c]i.g.: intragastric administration.

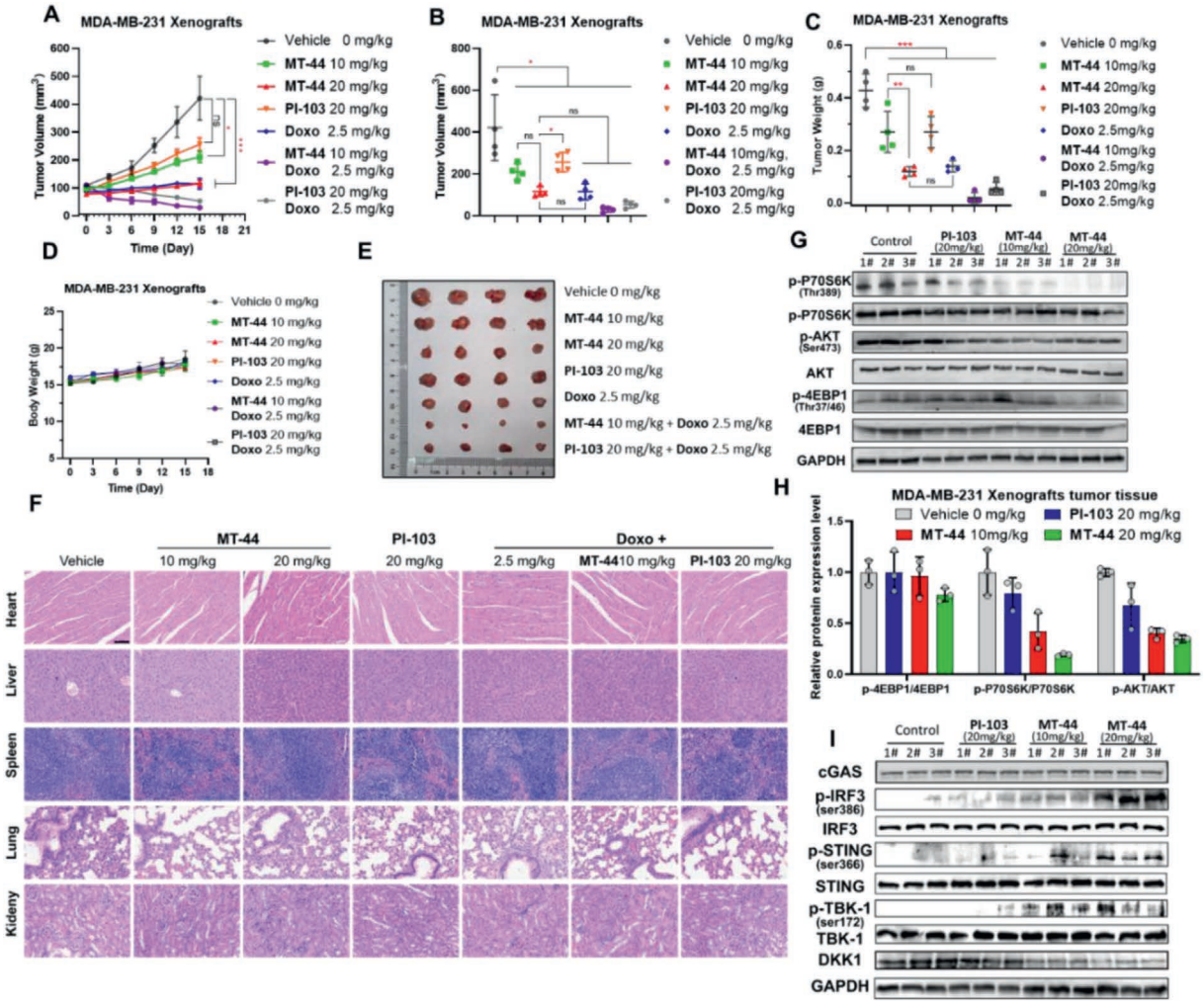

Figure 18 The xenograft tumor model was employed to assess the *in vivo* antitumor efficacy of **MT-44**. (A) Tumor volume growth curves for each treatment group. (B) Comparison of tumor volumes across groups on Day 15. (C) Comparison of tumor weights among groups on Day 15. (D) Body weight changes over time in each group, measured every three days to evaluate the safety profile of different treatments. (E) Tumors were excised from mice in all groups on Day 15. (F) H&E staining of major organs after treatment (scale bar = 100 μm). (G, H) The expression and quantitative analysis of mTOR signaling proteins in MDA-MB-231 cell xenografted mouse tumor tissues were analyzed using Western blotting. (I) The expression of cGAS/STING signaling pathway proteins in MDA-MB-231 cell xenografted mouse tumor tissue was detected using Western blotting.

(Proteintech, 10494-1-AP). After three 10-min TBST washes with gentle stirring, DyLight 800-coupled anti-rabbit IgG (H + L) secondary antibodies (1:15,000; Cell Signaling Technology) retarded buffering at 25 °C for 60 min. After incubation, the membrane was subjected to three rigorous 5-min washes with TBS containing 0.1% Tween-20 to eliminate non-specific binding.

4.12. Cellular thermal shift assay (CETSA)

The Cellular thermal shift assay (CETSA) was performed to evaluate target engagement of the test compound in living cells. Briefly, MDA-MB-231 cells were cultured to 70-80% confluence and treated with either the test compound (5 μmol/L, 8 h) or vehicle control (DMSO). After treatment, cells were harvested, washed with PBS, and subjected to a temperature gradient for 3 min each using a thermal cycler, followed by cooling to 25 °C for 3 min. Cells were then lysed in buffer containing 50 mmol/L Tris-HCl (pH 7.5), 150 mmol/L NaCl, 1% NP-40, and protease inhibitors, and insoluble aggregates were removed by centrifugation at 20,000×*g* for 15 min at 4 °C. Soluble proteins were quantified, separated by SDS-PAGE, and analyzed *via* immunoblotting using specific antibodies against the target protein. Band intensities were quantified using ImageJ software, and thermal stability curves were generated by plotting the percentage of soluble protein remaining versus temperature.

4.13. TLR2 reporter assay

The TLR2-agonistic activity of **MT-44, PI-103,** and Rapa was tested on TLR2 NFκB-Luc HEK293 reporter cells using an ultra luciferase detection kit (Co-bioer, Nanjing, China). Briefly, TLR2 NFκB-Luc HEK293 reporter cells were seeded into a 96-well plate at a density of 30,000 cells per well in medium (MEM + 10%FBS + 1%NEAA + 1 mmol/L NaP) containing different concentrations of **MT-44, PI-103,** and Rapa., respectively. After incubation for 6 h, added the ultra luciferase detection

Table 9 Tumor growth inhibition by **MT-44**, **PI-103**, and their combination therapy ($n = 4$).

Compd.	Treatment description	Tumor size (mm^3)[b]	*T/C* (%)	TGI (%)[c]
Vehicle	0 mg/kg, i.v., Q3D × 6	421.80 ± 136.31	–	–
MT-44	10 mg/kg, i.v., Q3D × 6	210.95 ± 33.18	61.36	38.64[d]
MT-44	20 mg/kg, i.v., Q3D × 6	115.97 ± 20.63	27.27	72.73[e]
PI-103	20 mg/kg, i.v., Q3D × 6	256.59 ± 40.06	61.36	38.64[d]
Doxo.[a]	2.5 mg/kg, i.v., Q7D × 2	115.17 ± 32.95	31.82	68.18[d]
MT-44 + Doxo.	10 mg/kg, i.v., Q3D × 6 2.5 mg/kg, i.v., Q7D × 2	29.66 ± 10.80	4.55	95.45[d]
PI-103 + Doxo.	10 mg/kg, i.v., Q3D × 6 2.5 mg/kg, i.v., Q7D × 2	53.27 ± 13.80	12.50	87.50[d]

TGI: tumor growth inhibition.
[a]Doxo. means Doxorubicin.
[b]Mean ± SEM.
[c]Compared with the vehicle group on Day 15 using ordinary one-way ANOVA.
[d]$P < 0.0001$.
[e]$P = 0.0001$ (one-way ANOVA).

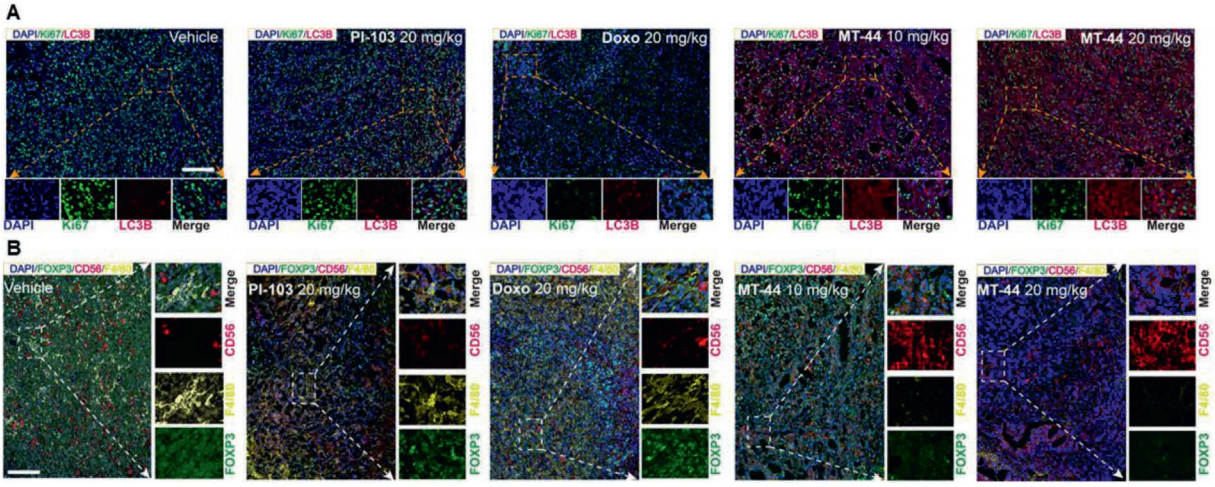

Figure 19 Compound **MT-44** enhances immune infiltration in the tumor environment. (A) Immunofluorescence analysis of Ki67 (green) and LC3B (red) expression in tumor tissue, the nucleus was stained with DAPI (blue). (B) The expression of FOXP3 (green), CD56 (red), and F4/80 (yellow) in tumor tissues was analyzed using immunofluorescence, and the nucleus was stained with DAPI (blue, scale bar = 100 μm). Data are expressed as mean ± SD ($n = 4$); *$P < 0.05$, **$P < 0.01$. ns, not significant.

kit and measured the absorbance using a plate reader. TLR2 agonist Pam3CSK4 was used as a positive control. The EC_{50} values were calculated using GraphPad Prism 8.3.

4.14. Metabolic stability study

4.14.1. Simulated gastrointestinal fluid stability study

Artificial gastrointestinal fluids were prepared according to the Chinese Pharmacopoeia (2020 edition). **MT-44** (10 mg/mL, containing 1% organic solvent) was incubated with blank gastric fluid, simulated gastric fluid (SGF), blank intestinal fluid, and simulated intestinal fluid (SIF) at 37 °C. Reactions were terminated at 0, 0.5, 1, 2, 4, and 6 h by adding 400 μL of ice-cold methanol. The mixtures were vortex-mixed for 5 min and centrifuged at 13,000 rpm for 10 min at 4 °C. Supernatants were collected for analysis, and the peak area of **MT-44** was recorded. The residual percentage of **MT-44** at each time point was calculated relative to the initial drug content (0 h, defined as 100%).

4.14.2. Plasma stability assay

Blank SD rat plasma (198 μL) was mixed with 2 μL of **MT-44** (containing 1% organic solvent) and incubated at 37 °C. Reactions were quenched at 0, 0.5, 1.0, 2.0, and 3.0 h by adding 600 μL of ice-cold methanol. After vortex-mixing for 5 min, samples were centrifuged at 13,000 rpm for 10 min at 4 °C. The supernatants were collected, dried under an N_2 stream, and reconstituted with 200 μL methanol. Following centrifugation (13,000 rpm, 10 min), the supernatants were analyzed.

4.14.3. Liver microsomal metabolic stability evaluation

MT-44 (10 μg/mL) was pre-incubated with rat liver microsomes (0.5 mg/mL) at 37 °C for 5 min. The reaction was initiated by adding an NADPH-regenerating system (1 mmol/L), and aliquots were collected at 0, 5, 10, 15, 30, 45, and 60 min. Reactions were terminated with 600 μL ice-cold methanol, vortex-mixed for 5 min, and centrifuged at 13,000 rpm for 10 min at 4 °C. Supernatants were dried under N_2 at 37 °C, reconstituted in 200 μL

methanol, and centrifuged again (13,000 rpm, 10 min) prior to analysis.

4.15. Pharmacokinetic study

Ten SD rats (220 ± 20 g) were randomly divided into two groups ($n = 5$ per group). Mice were treated with the **MT-44** drug at a dose of 5 mg per kg of body weight *via* the tail vein. Then, the blood samples were collected from the inner canthus vein plexus at 0.05, 0.25, 0.5, 1, 2, 4, 8, 12, 16, 24, and 30 h after intravenous administration. Another group of mice was treated with the **MT-44** drug at a dose of 20 mg per kg of body weight oral. Then, the blood samples were collected from the inner canthus vein plexus at 0.25, 0.5, 0.75, 1, 2, 4, 6, 8, 12, 16, 24, and 30 h after intravenous administration, which were immediately centrifuged (3000 rpm) at 4 °C for 10 min. The plasma was analyzed on an AB SCIEX Instruments 5500 triple quadrupole mass spectrometer (Applied Biosystems, Foster City, CA) interfaced online with a 1290 infinity system (Agilent Technologies, Santa Clara, CA). The concentration-time profiles were plotted using GraphPad Prism 8.0.2 software. Pharmacokinetic parameters were calculated using DAS 2.0.

For intravenous (i.v.) administration, the concentration of **MT-44** in plasma samples collected at 0.05, 0.25, and 0.5 h after i.v. administration was found to be higher than the upper limit of quantification. Plasma samples collected at 0.05, 0.25, and 0.5 h after i.v. administration were diluted once with blank plasma (20 μL of plasma samples added to 80 μL of blank plasma) before preparation; plasma samples collected after 0.5 h were prepared as aforementioned.

4.16. Evaluation of in vivo anti-tumor efficacy

All animal experiments were conducted under the guidance and supervision of the Animal Ethics Committee of Guizhou University (Approval No. SYXK (Gui) 2025-0001). To evaluate the anti-tumor effect of **MT-44** *in vivo*, we established a xenograft tumor model using MDA-MB-231 cells in female BALB/c nude mice. Three-week-old female BALB/c nude mice were purchased from Beijing Vital River Laboratory Animal Technology Co., Ltd. and acclimated in a specific pathogen-free environment for 3 days. MDA-MB-231 cells in the logarithmic growth phase were harvested and resuspended in physiological saline to a concentration of 1×10^7 cells per milliliter. One hundred microliters of the cell suspension were injected subcutaneously into the right fat pad of each mouse. When the average tumor volume reached approximately 100 mm^3, the mice were randomly divided into seven groups ($n = 4$ per group): (A) physiological saline control; (B) **MT-44** at 10 mg/kg; (C) **MT-44** at 20 mg/kg; (D) **PI-103** at 20 mg/kg as a positive control; (E) doxorubicin at 2.5 mg/kg as a positive control; (F) combination of **MT-44** at 10 mg/kg and doxorubicin at 2.5 mg/kg; (G) combination of **PI-103** at 20 mg/kg and doxorubicin at 2.5 mg/kg. All pharmacological agents were administered through intravenous injection *via* the tail vein. Tumor dimensions were measured every 3 days using calipers, and body weight was recorded simultaneously. Tumor volume was calculated using Eq. (1):

$$V = Length \times Width^2 \times 0.5 \quad (1)$$

On Day 15, all mice were euthanized using isoflurane (Shenzhen, China).

4.17. H&E staining

Tissue samples, including heart, liver, spleen, lung, and kidney, were collected from mice in each experimental group. The specimens were fixed in 4% paraformaldehyde (Beyotime, Shanghai, China) and embedded in paraffin. Serial sections (4 μm thickness) were prepared and subjected to hematoxylin and eosin (H&E) staining. Histopathological evaluation was performed through light microscopic examination to assess morphological alterations.

4.18. Immunofluorescence staining

MDA-MB-231 cells were cultured in confocal dishes until they reached about 80% confluence. Subsequently, the cells were assigned to different groups and given the corresponding concentration of the compound, and the solvent dose of DMSO as a control. After treatment, the cells were fixed with 4% paraformaldehyde overnight and then permeated on ice with 0.2% Triton X-100 for 20 min. Then rinse with 0.01 mol/L phosphate-buffered saline three times for 10 min. The cells were then sealed with 2% bovine serum albumin at room temperature for 1 h, washed with PBS 3 times (10 min each time), and treated with rabbit primary antibody. On the second day, Alexa Fluor 488 Goat anti-rabbit antibody (Proteintech) was administrated at room temperature for 1 h, then washed 3 times with 0.01 mol/L PBS. After immobilization in a DAPI-containing medium and 3 additional washes of PBS, the cells were subjected to ZEISS LSM 900 (CLSM, Jena, Germany) for 3D reconstruction.

4.19. Statistical analysis

Data were analyzed using GraphPad Prism 8.3 with parametric statistical approaches. Continuous variables are expressed as mean ± Standard deviation (SD). For comparisons involving three or more experimental groups, one-way ANOVA followed by Dunnett's *post hoc* test was applied to adjust for multiple comparisons. A two-tailed $P < 0.05$ defined statistical significance. Sigmoidal dose-response modeling was employed to calculate median inhibitory concentrations (IC_{50}), with graphical outputs generated directly through the software's nonlinear regression module. Data are expressed as mean ± SD. All data are representative of at least three independent experiments. $^*P < 0.05$; $^{**}P < 0.01$; $^{***}P < 0.001$; $^{****}P < 0.0001$. ns, not significant.

Acknowledgments

This work was financially supported by the Natural Science Foundation of China (22267003), the Guizhou Provincial Basic Research Program (Natural Science) (ZK[2023]305, ZK[2024]170, China), the Guizhou Provincial Excellent Young Talents Plan (YQK[2023]030, China), the Guizhou Provincial Major Scientific and Technological Program ([2024]015, China), the Natural Science Foundation of Guangdong Province (No. 2023B1515020042, China), and the Excellent Young Talents Plan of Guizhou Medical University ([2022]102, China).

Author contributions

Ji-Quan Zhang, Lei Tang, Changyou Zhan, and Ling Wang, as the supervisors, conceived the project and supplied the financial support. Nana Zhang, Jiangrong Lu, Yuanyong Yang, and Rong-

Hua Wang conducted the synthesis of compounds. Yunsheng Ran, Qi-Ying Yu, Yuanyuan Li, and Rui Chen conducted the activity assays. Yongxi Dong and Weike Liao did the data analysis. Nana Zhang and Shipeng Zhang conducted virtual screening, machine learning, molecular docking, and molecular dynamics simulation. Ji-Quan Zhang, Nana Zhang, and Changyou Zhan wrote and edited the manuscript. All authors read and approved the final manuscript.

Conflicts of interest

The authors have no conflicts of interest to declare.

Appendix A. Supporting information

Supporting information to this article can be found online at https://doi.org/10.1016/j.apsb.2025.09.010.

References

1. Waks AG, Winer EP. Breast cancer treatment: a review. *J Am Med Assoc* 2019;**321**:288−300.
2. Foulkes WD, Smith IE, Reis-Filho JS. Triple-negative breast cancer. *N Engl J Med* 2010;**363**:1938−48.
3. Bianchini G, De Angelis C, Licata L, Gianni L. Treatment landscape of triple-negative breast cancer-expanded options, evolving needs. *Nat Rev Clin Oncol* 2022;**19**:91−113.
4. Liao MR, Zhang J, Wang G, Wang LM, Liu J, Ouyang L, et al. Small-molecule drug discovery in triple negative breast cancer: current situation and future directions. *J Med Chem* 2021;**64**:2382−418.
5. Liu PX, Cheng HL, Roberts TM, Zhao JJ. Targeting the phosphoinositide 3-kinase pathway in cancer. *Nat Rev Drug Discov* 2009;**8**: 627−44.
6. Saxton RA, Sabatini DM. mTOR signaling in growth, metabolism, and disease. *Cell* 2017;**168**:960−76.
7. Li X, Chen KQ, Wang ZX, Li JY, Wang XW, Xie C, et al. The mTOR signalling in corneal diseases: a recent update. *Biochem Pharmacol* 2023;**213**:115620.
8. Zhu SL, Wu YZ, Song B, Yi M, Yan YH, Mei Q, et al. Recent advances in targeted strategies for triple-negative breast cancer. *J Hematol Oncol* 2023;**16**:100.
9. Zhang HP, Jiang RY, Zhu JY, Sun KN, Huang Y, Zhou HH, et al. PI3K/AKT/mTOR signaling pathway: an important driver and therapeutic target in triple-negative breast cancer. *Breast Cancer* 2024;**31**:539−51.
10. Xiang HG, Zhang JF, Lin CC, Zhang L, Liu B, Ouyang L. Targeting autophagy-related protein kinases for potential therapeutic purpose. *Acta Pharm Sin B* 2020;**10**:569−81.
11. Liu H-J, Du H, Khabibullin D, Zarei M, Wei K, Freeman GJ, et al. mTORC1 upregulates B7-H3/CD276 to inhibit antitumor T cells and drive tumor immune evasion. *Nat Commun* 2023;**14**(1):1214.
12. Chi H. Regulation and function of mTOR signalling in T cell fate decisions. *Nat Rev Immunol* 2012;**12**(5):325−38.
13. Corrales L, McWhirter SM, Dubensky Jr TW, Gajewski TF, Gajewski TF. The host STING pathway at the interface of cancer and immunity. *J Clin Investig* 2016;**126**:2404−11.
14. Woo SR, Fuertes MB, Corrales L, Spranger S, Furdyna MJ, Leung MYK, et al. STING-dependent cytosolic DNA sensing mediates innate immune recognition of immunogenic tumors. *Immunity* 2014;**41**:830−42.
15. Deng LF, Liang H, Xu M, Yang XM, Burnette B, Arina A, et al. STING-dependent cytosolic DNA sensing promotes radiation-induced type I interferon-dependent antitumor immunity in immunogenic tumors. *Immunity* 2014;**41**:843−52.
16. Samson N, Ablasser A. The cGAS-STING pathway and cancer. *Nat Cancer* 2022;**3**:1452−63.
17. Chen C, Xu PL. Cellular functions of cGAS-STING signaling. *Trends Cell Biol* 2023;**33**:630−48.
18. Dou ZX, Ghosh K, Vizioli MG, Zhu JJ, Sen P, Wangensteen KJ, et al. Cytoplasmic chromatin triggers inflammation in senescence and cancer. *Nature* 2017;**550**:402−6.
19. Lu HL, Yang Y, Gad E, Inatsuka C, Wenner CA, Disis ML, et al. TLR2 Agonist PSK activates human NK cells and enhances the antitumor effect of HER2-targeted monoclonal antibody therapy. *Clin Cancer Res* 2011;**17**:6742−53.
20. Keenan TE, Tolaney SM. Role of immunotherapy in triple-negative breast cancer. *J Natl Compr Cancer Netw* 2020;**18**:479−89.
21. Khan MA, Jain VK, Rizwanullah M, Ahmad J, Jain K. PI3K/AKT/mTOR pathway inhibitors in triple-negative breast cancer: a review on drug discovery and future challenges. *Drug Discov Today* 2019;**24**:2181−91.
22. Jovanovic B, Mayer IA, Mayer EL, Abramson VG, Bardia A, Sanders ME, et al. A randomized phase II neoadjuvant study of cisplatin, paclitaxel with or without everolimus in patients with stage II/III triple-negative breast cancer (TNBC): responses and long-term outcome correlated with increased frequency of DNA damage response gene mutations, TNBC subtype, AR status, and Ki67. *Clin Cancer Res* 2017;**23**:4035−45.
23. Singh J, Novik Y, Stein S, Volm M, Meyers M, Smith J, et al. Phase 2 trial of everolimus and carboplatin combination in patients with triple negative metastatic breast cancer. *Breast Cancer Res* 2014;**16** (R32/1).
24. Jang NY, Kim DH, Cho BJ, Choi EJ, Lee JS, Wu HG, et al. Radiosensitization with combined use of olaparib and PI-103 in triple-negative breast cancer. *BMC Cancer* 2015;**15**:1−9.
25. Torki S, Soltani A, Shirzad H, Esmaeil N, Ghatrehsamani M. Synergistic antitumor effect of NVP-BEZ235 and CAPE on MDA-MB-231 breast cancer cells. *Biomed Pharmacother* 2017;**92**:39−45.
26. Davis SL, Ionkina AA, Bagby SM, Orth JD, Gittleman B, Marcus JM, et al. Preclinical and dose-finding phase I trial results of combined treatment with a TORC1/2 inhibitor (TAK-228) and aurora A kinase inhibitor (Alisertib) in solid tumors. *Clin Cancer Res* 2020;**26**:4633−42.
27. Xu T, Sun DJ, Chen Y, Ouyang L. Targeting mTOR for fighting diseases: a revisited review of mTOR inhibitors. *Eur J Med Chem* 2020; **199**:112391.
28. Paul D, Sanap G, Shenoy S, Kalyane D, Kalia K, Tekade RK. Artificial intelligence in drug discovery and development. *Drug Discov Today* 2021;**26**:80−93.
29. Gangwal A, Lavecchia A. Unleashing the power of generative AI in drug discovery. *Drug Discov Today* 2024;**29**:103992.
30. Gangwal A, Lavecchia A. AI-driven drug discovery for rare diseases. *J Chem Inf Model* 2025;**65**:2214−31.
31. Cai HX, Zhang HM, Zhao DC, Wu JX, Wang L. FP-GNN: a versatile deep learning architecture for enhanced molecular property prediction. *Briefings Bioinf* 2022;**23**:1−12.
32. Sun QW, Chu YX, Zhang NN, Chen R, Wang LL, Wu JX, et al. Design, synthesis, formulation, and bioevaluation of trisubstituted triazines as highly selective mTOR inhibitors for the treatment of human breast cancer. *J Med Chem* 2024;**67**:7330−58.
33. Zhang JQ, Luo YJ, Xiong YS, Yu Y, Tu ZC, Long ZJ, et al. Design, synthesis, and biological evaluation of substituted pyrimidines as potential phosphatidylinositol 3-kinase (PI3K) inhibitors. *J Med Chem* 2016;**59**:7268−74.
34. Wu CF, Wang QC, Chen R, Zhou HL, Wu TT, Du Y, et al. Synthesis and bioevaluation of diaryl urea derivatives as potential antitumor agents for the treatment of human colorectal cancer. *Eur J Med Chem* 2022;**229**:114055.
35. Zhang NN, Ban YJ, Wang YJ, He SY, Qi PP, Bi T, et al. Virtual screening of novel mTOR inhibitors for the potential treatment of human colorectal cancer. *Bioorg Chem* 2023;**140**:106781.
36. Huang JD, Chen LY, Wu JX, Ai DQ, Zhang JQ, Chen TG, et al. Targeting the PI3K/AKT/mTOR signaling pathway in the treatment of human diseases: current status, trends, and solutions. *J Med Chem* 2022;**65**:16033−61.

37. Liu SC, Alnammi M, Ericksen SS, Voter AF, Ananiev GE, Keck JL, et al. Practical model selection for prospective virtual screening. *J Chem Inf Model* 2019;**28**(59):282−93.
38. Zheng XM, Chen YS, Ban YJ, Wang YJ, Dong YX, Lei L, et al. Design, synthesis and bioevaluation of PI3Kα-selective inhibitors as potential colorectal cancer drugs. *Eur J Med Chem* 2023;**260**:115754.
39. Borsari C, De Pascale M, Wymann MP. Chemical and structural strategies to selectively target mTOR kinase. *ChemMedChem* 2021; **16**:2744−59.
40. Hua H, Kong QB, Zhang HY, Wang J, Luo T, Jiang YF. Targeting mTOR for cancer therapy. *J Hematol Oncol* 2019;**12**:71.
41. Friedl P, Wolf K. Tumor-cell invasion and migration: diversity and escape mechanisms. *Nat Rev Cancer* 2003;**3**:362−74.
42. Fares J, Fares MY, Khachfe HH, Salhab HA, Fares Y. Molecular principles of metastasis: a hallmark of cancer revisited. *Signal Transduct Targeted Ther* 2020;**5**:28.
43. Carneiro BA, El-Deiry WS. Targeting apoptosis in cancer therapy. *Nat Rev Clin Oncol* 2020;**17**:395−417.
44. Solier S, Pommier Y. The nuclear γ-H2AX apoptotic ring: implications for cancers and autoimmune diseases. *Cell Mol Life Sci* 2014;**71**: 2289−97.
45. Xu ZR, Han X, Ou DM, Liu T, Li ZX, Jiang GM, et al. Targeting PI3K/AKT/mTOR-mediated autophagy for tumor therapy. *Appl Microbiol Biotechnol* 2020;**104**:575−87.
46. Poillet-Perez L, Despouy G, Delage-Mourroux R, Boyer-Guittaut M. Interplay between ROS and autophagy in cancer cells, from tumor initiation to cancer therapy. *Redox Biol* 2015;**4**: 184−92.
47. Qiao SX, Dennis M, Song XF, Vadysirisack DD, Salunke D, Nash Z, et al. A REDD1/TXNIP pro-oxidant complex regulates ATG4B activity to control stress-induced autophagy and sustain exercise capacity. *Nat Commun* 2015;**6**:7014.
48. Zhang ZL, Zhou HF, Ouyang XH, Dong YL, Sarapultsev A, Luo SS, et al. Multifaceted functions of STING in human health and disease: from molecular mechanism to targeted strategy. *Signal Transduct Targeted Ther* 2022;**7**:394.
49. Andrs M, Korabecny J, Jun D, Hodny Z, Bartek J, Kuca K. Phosphatidylinositol 3-Kinase (PI3K) and phosphatidylinositol 3-kinase-related kinase (PIKK) inhibitors: importance of the morpholine ring. *J Med Chem* 2015;**58**:41−71.
50. Michino M, Beautrait A, Boyles NA, Nadupalli A, Dementiev A, Sun S, et al. Shape-based virtual screening of a billion-compound library identifies mycobacterial lipoamide dehydrogenase inhibitors. *ACS Bio & Med Chem Au* 2023;**3**:507−15.
51. Zhang NN, Bai X, Zhao SS, Zheng XM, Tang L, Yang SG, et al. Computational study reveals substituted benzimidazole derivatives' binding selectivity to PI3Kδ and PI3Kγ. *J Mol Model* 2022;**28**:123.